
Politecnico di Torino

Dipartimento di Ingegneria Meccanica e Aerospaziale

Course of **Master of Science in Mechanical Engineering**

Thesis on

**Laser Powder Bed Fusion of CuNi₂SiCr alloy:
Process parameters optimization and electro-
mechanical characterization**



Supervisors

Prof. Federica Bondioli

Dr. Elisa Padovano

Matteo Vanzetti

Candidate

Rohan Polkam (274807)

October 2022

Abstract

Among metals, copper has one of the highest values of electrical and thermal conductivities, second only to silver. These properties, in addition to a good corrosion resistance and ease of both extraction from ore and fabrication, make copper a promising candidate for many applications including the use of this material for heat exchangers. Other applications are in electronics, pipes and fittings, automotive and electrical industries. The increasing ability of Additive Manufacturing (AM) technologies to process metals in past decades, has diversified this expanse of applications. AM has been applied to increase the efficiency of the already existing applications of copper like induction-coils while also creating new potential application-areas, for example, production of rocket engine nozzles. This has enhanced the performance of the products multi-fold and made the otherwise expensive technology, economically feasible. Also, copper alloys are known to have a good blend of moderate physical strength, electrical and thermal conductivities. It makes them desirable to use in harsh environments where a combination of the properties is necessary. This thesis focuses on CuNi₂SiCr alloy, which exhibits high corrosion resistance, creep resistance, wear resistance and high stiffness at elevated temperatures. These properties are exploited in applications such as tooling-inserts, valves and brackets/fixtures. The absence of extensive research on this particular alloy in the field of AM, increases the need to investigate its characteristics. Test samples were manufactured from pre-alloyed powder using Laser Powder Bed Fusion (LPBF) technique equipped with a laser with wavelength in the near-infrared range. Test-samples were printed using different sets of machine process parameters (scanning speed, hatching distance and layer thickness) to find the optimal combination that yields the highest relative density. The limited power of the LPBF machine used (Concept Laser Mlab R), coupled with the high thermal conductivity and low absorption of copper leads to microstructure with residual porosity (around 3 %). Subsequently, a batch of samples were fabricated using the optimized process parameters and relative densities above 97% were obtained. To observe different aspects of the microstructure, namely grains and melt-pools, various etchants were applied to the polished-test samples. Microscopic analysis also hinted towards presence of oxides in the defects. An upward trend of relative densities was observed for samples with increasing cross-sectional areas, which can be an interesting research area for future studies.

Acknowledgements

First and foremost, I would like to thank my parents who have been instrumental in allowing me to reach this important milestone of my life. Secondly, I would like to thank the professors at Politecnico di Torino who have guided me through these past few years and provided me with their invaluable knowledge and time.

I would like to express my gratitude to Prof. Federica Bondioli, Dr. Elisa Padovano and Matteo Vanzetti for their continued support, understanding and the knowledge they have imparted to me throughout the duration of this thesis.

Thank you to my family, friends and colleagues for encouraging me to do my best! Thank you to anyone who influenced me during these years in one way or another!

Table of Contents

1. INTRODUCTION	1
1.1 Background and current trends of Additive Manufacturing (AM)	1
1.2 Advantages of AM over traditional methods	2
1.3 Limitations of AM	3
2. CLASSIFICATION OF METAL AM TECHNIQUES	4
2.1 Laser Powder Bed Fusion (LPBF)	4
2.2 Electron Beam Powder Bed Fusion	7
2.3 Directed Energy Deposition	8
3. COPPER AND ITS ALLOYS FOR AM	10
3.1 Copper and its alloys used for traditional manufacturing methods	10
3.2 Copper Alloys currently used in AM	11
3.2.1 CuNi2SiCr (C18000)	13
4. EQUIPMENTS USED FOR CHARACTERISATION OF POWDER	16
4.1 Flowability measurement	16
4.2 Density measurement	17
4.2.1 Tapped Density	17
4.2.2 Gas Pycnometer	18
4.3 Dimension measurement	19
5. PRODUCTION OF TEST SAMPLES	21
6. EQUIPMENTS USED FOR CHARACTERISATION OF TEST SAMPLES	24
6.1 Sample Cutting Machine	24
6.2 Density measurement	25
6.3 Metallographic compression mounting machine	25
6.4 Polishing machine	26
6.5 Optical microscope (OM)	27
6.5.1 Image analysis using <i>ImageJ</i> software	27
6.6 Scanning Electron Microscope (SEM)	28
6.6.1 Energy Dispersive X-ray Spectroscopy (EDS or EDX)	30
6.7 X-Ray Diffractometry (XRD)	30
6.8 Vickers Hardness Tester	31
6.9 Universal Testing Machine (UTM)	32
6.10 Electrical Conductivity test	33
7. RESULTS AND DISCUSSION	34

7.1	Powder Characterization	34
7.1.1	Flowability	35
7.1.2	Density	36
7.1.3	Particle size distribution.....	37
7.2	Test Samples Characterisation.....	38
7.2.1	Relative Density	38
7.2.2	Microstructure	41
7.2.3	Physical properties.....	50
8.	CONCLUSION	54

List of Figures

Figure 1: Classification of Metal AM Technologies [10]	4
Figure 2: LPBF Working Principle	5
Figure 3: EBM working principle [19].....	8
Figure 4: DED Working Principle [20].....	9
Figure 5: Copper-Nickel Phase diagram [30].....	14
Figure 6: Microstructure of C18000 at 30X magnification [31]	14
Figure 7: Hall Flowmeter Apparatus [34].....	16
Figure 8: Gas Pycnometer Working Principle [35]	19
Figure 9: Anton Paar Pycnometer (Model: Ultrapyc 5000) [36]	19
Figure 10: Laser Diffraction Granulometry Working Principle [40]	20
Figure 11: Granulometer Malvern Panalytical (Model: Mastersizer 3000) [41].....	20
Figure 12: Concept Laser Mlab LPBF system (Model: R) [42]	21
Figure 13: Job 1 printed samples with build-plate.....	22
Figure 14: Job 2 printed samples with build-plate.....	22
Figure 15: Job 3 printed samples with dog-bone tensile samples.....	23
Figure 16: Job 4 printed samples	23
Figure 17: QATM Precision Cut-off machine (Model: Brilliant 220) [52].....	24
Figure 18: Sample cut-off from build-plate.....	24
Figure 19: Remet compression mounting press (Model: IPA 30) [53].....	25
Figure 20: Sample encapsulated in resin	25
Figure 21: Presi automatic polishing machine (Model: Mecatech 234) [54].....	26
Figure 22: Leica DMI Optical Microscope (Model: 5000M) [55].....	27
Figure 23: Image obtained from Optical Microscope	27
Figure 24: Setting threshold in ImageJ.....	28
Figure 25: Detected porosity	28
Figure 26: Working principle of SEM [56]	29
Figure 27: Alfastest Scanning Electron Microscope (Model: Phenom XL G2) [57].....	29
Figure 28: EDS working principle [58].....	30
Figure 29: XRD working principle [59]	31
Figure 30: X-ray diffractometer from Malvern Panalytical (Model: Empyrean) [60]	31
Figure 31: Vickers Hardness Test working [61].....	32
Figure 32: Micro-vickers Hardness Tester from Chongqing Scope Instruments (Model: DHV-1000) [62]	32
Figure 33: Zwick Roell UTM (Model: Z100) [63]	33
Figure 34: 4-point electrical conductivity test [64].....	33
Figure 35: SEM images of procured powder.....	35
Figure 36: OM image of encapsulated powder (Magnification: 200X).....	37
Figure 37: PSD of procured powder	37
Figure 38: Relative density variation with Scanning speed	38
Figure 39: Relative density variation with Volumetric Energy Density.....	39
Figure 40: Relative density variation for Job 3.....	40
Figure 41: Relative density variation in Job 4 samples with single-pass of laser.....	41
Figure 42: Job 1-Sample 1 OM image analysed with ImageJ software (Magnification: 50X).....	42
Figure 43: Job 1-Sample 8 OM image analysed with ImageJ software (Magnification: 50X).....	42
Figure 44: Job 3-Sample "D" OM image analysed with ImageJ software (Magnification: 50X)	43

Figure 45: EDS Map Analysis	44
Figure 46: EDS Map Analysis	44
Figure 47: EDS Spot Analysis	45
Figure 48: EDS Spot Analysis	45
Figure 49: Melt-pool visualization (Magnification: 500X).....	46
Figure 50: Columnar grain structure (Magnification: 200X)	47
Figure 51: Columnar grain structure (Magnification: 500X)	47
Figure 52: SEM images after etching (Magnification: 5000X)	48
Figure 53: Un-melted powder (Magnification: 500X).....	48
Figure 54: Un-melted powder and cracks (Magnification: 500X)	49
Figure 55: XRD Output graph	49
Figure 56: Tensile test plots	51
Figure 57: Effect of relative density on electrical conductivity of pure copper produced with AM [26]	52
Figure 58: Test for homogeneity.....	53

List of Tables

Table 1: UNS Copper and Copper Alloys families [21]	10
Table 2: Copper alloys currently used in AM [26].....	12
Table 3: CuNi2SiCr composition.....	13
Table 4: Flowability characteristics of powder [36].....	18
Table 5: Concept Laser Mlab R - Technical Specifications [43].....	21
Table 6: Jobs 1 and 2 process parameters	22
Table 7: CuNi2SiCr composition as per datasheet provided by Praxair Surface Technologies	34
Table 8: Bulk and Tapped Density of Powder	36
Table 9: Compressibility Index and Hausner Ratio of powder.....	36
Table 10: PSD of powder.....	37
Table 11: Process parameters of the sample with highest relative density	38
Table 12: Element concentrations inside map of Figure 45	44
Table 13: Element Concentrations inside map of Figure 46.....	44
Table 14: Element concentrations in spot of Figure 47	45
Table 15: Element concentrations in spot of Figure 48	45
Table 16: Tensile test values	50
Table 17: Tensile test values reported in datasheet of SLM Solutions [29]	50
Table 18: Tensile test values reported in datasheet of CRP Meccanica [67].....	51
Table 19: Hardness test values reported in datasheet of SLM Solutions [29].....	51
Table 20: Electrical conductivity value reported in datasheet of SLM Solutions [29]	52

1. INTRODUCTION

1.1 Background and current trends of Additive Manufacturing (AM)

Additive manufacturing (AM) is a relatively new technology as compared to the conventional machining processes of turning, milling, fabrication and casting. Nowadays, a large portion of metal-components in the industries are produced using these traditional techniques; many of them are subtractive manufacturing techniques, wherein material is removed using tools from blocks of metal called billets. On the other hand, AM, as the name suggests, builds a component by adding one layer of material above other. Its conception took place in the 1980s with the invention of Stereolithography (SLA) [1], which used a laser to solidify a photo-sensitive liquid polymer. It was one of the first types of AM. Many of the primitive versions of SLA, and other AM methods such as Fused Deposition Modelling and Binder Jetting focused on plastics. Back then the colloquial term for the pool of these processes was 3D-printing, and to an extent, for the broad range of techniques of AM it still is. They were mainly used for making prototypes due to the constraint of slow print-speed of the printers. Owing to this application, this type of manufacturing was also called Rapid Prototyping. Coming up to 1990s with the advent of metals in the world of AM, the application field diversified. The processes were now used to create custom and flexible tooling, tooling inserts, jigs and fixtures, as a result of which the processes became known as Rapid Tooling [2]. By 2000s however, after recognizing the advantages of AM, several companies showed interest in enhancing existing techniques and developing novel technologies for producing end-usable parts using metal-AM; therefore/with this aim, corporate investments started pouring into research institutions and laboratories. Along with that world was seeing exponential increase in computing power of processors. The modelling of a component to be produced moved from 2D hand-drafting to 3D Computer Aided Design (CAD) models. This paved the way for the improvement and development of a variety of metal-AM technologies and an extra degree of freedom for a design-engineer to bring the design into reality.

AM is set to play a major role in Industry 4.0 as its themes of information transparency and decentralized decisions by machines can be implemented more readily as compared to other techniques. The role of AM in aerospace and automotive markets has been steadily growing and is predicted to grow by around 20% in the next decade [3]. The costs of producing a component with AM have decreased over the last 5 years [4] and will continue to decrease with the raw material being more and more readily available; moreover, the initial investments for AM companies decreasing with decreasing costs of AM machines and the growing printing-speeds of these machines.

1.2 Advantages of AM over traditional methods

The flexibility with which complex-components can be manufactured using AM, is its biggest asset over other methods. The cutting tools of the subtractive machining processes cannot produce hollow regions in a part as they cannot reach those regions; on the other hand, formative processes like casting can produce cavities with the use of cores, but the complexity of these cavities is limited. Whereas, with the help of AM negative spaces as complicated as lattice structures are a promising possibility. Components with lattice structures generally have higher strength-to-weight ratio than solid ones due to effective handling of external forces and even stress-distribution across the component [5]. AM also leads to flexibility in changing designs of tooling. Around 60% of design-changes occur during the production of tools, which requires significant costs and time [4]. AM can provide that degree of freedom for designers of iterating that amounts to only a fraction of the company's time and resources.

Weight-saving can be performed by reducing the number of components in an assembly. The ability to produce complex shapes and internal-hollow structures also introduces the advantage of integrated assemblies. It eliminates the need for the use of joint and fasteners, which increases the reliability of the component, reduces the assembly time and the labor cost as less operators are needed for assembly. The process itself requires very less operator intervention. Initial setting of the parameters requires some operator attention, but once the sample products are up to the required standards, same parameters can be utilized to produce innumerable parts of the same shape, size and dimensions without needing operator supervision or intervention. [6]

The use of AM for rapid prototyping also translates to lower lead-time because it does not require expensive tooling changes. For example, in case of casting or stamping, firstly a die has to be manufactured consuming precious time and resources. Also, in case of design changes in the product or changes in customer requirements. the die has to be designed from scratch. Whereas in case of AM, only tweaks in CAD model will do the trick. For low and medium volume production, AM facilitates not having to do a large initial investment in tooling for traditional manufacturing machines. It is more feasible for companies, as the primary reason they prefer large volume production, is that they are limited by logistic costs.

AM allows companies to manufacture close to their clients, thus companies can avoid storing a buffer of products reducing the resources used for them. During the Covid-19 pandemic, the disruption of global supply-chain meant huge losses for companies sourcing their raw-material or inventory internationally. The shortcomings of globalization became apparent during this period. On the other hand, industries using local resources, for example, having suppliers in their vicinity or industries which predominantly use AM machines did not depend on the global network and hence could keep their production-line running [7].

1.3 Limitations of AM

Currently, the major limitation hampering AM's widespread adaptation in the market is the limited build-volume of AM machines. Most AM Machines that are available in the market, have/show a build envelope with dimensions of the order of half a meter. This can be a limit because most CNC machines are capable of working on components which can work on components that are 3 to 4 times larger in dimension with respect to AM parts. Where the largest dimensions of an AM part are limited by the build envelope, the smallest dimensions are limited by the raw-material and the type of AM system used.

Where AM is advantageous for low and medium volume productions, it has its limitations for high-volume productions. The main limiting factor is the speed of AM machines. Currently most AM machines have maximum scanning speeds close to 7 m/s, but unless this value is ramped-up quite a bit the preferred technique for large-scale production would be traditional manufacturing methods. In fact, even though traditional techniques require more lead-time, when the quantity of products to be manufactured is high enough, their production through traditional methods is generally faster with respect to the time required for processing the same number of components by AM techniques. [4]

The portfolios of AM machines include relatively less materials as compared to the materials that can be processed using traditional manufacturing techniques. This is particularly an issue for metals. The type of power source restricts the type of metal that can be used. This eliminates a large portion of alloys which have attractive physical properties and potential applications [8]. As discussed in Section 2, majority of AM techniques currently in use for metals are Laser Powder Bed Fusion (LPBF) and Electron Beam Melting (EBM). Only conductive materials can be processed using EBM, because the metal-powder needs to interact with the electrons in electron-beam. Hence, most EBM machine manufacturers only have selective materials of titanium alloys and copper alloys in their portfolio. In case of LPBF, the absorptivity of different metals varies with the wavelength of laser used. For example, gold and silver have an absorptivity of 0.03% at 1064 nm [9], the wavelength of laser used by most LPBF systems and hence components with such metals can't be produced using this technology.[8]

Porosity is inevitable in a component produced with AM, due to its working principle. The pores adversely affect the physical properties of the component like yield strength, ultimate tensile strength, elongation at break, electrical conductivity. The randomness of the pores also introduces anisotropy of properties. This anisotropy can also be due to uneven heat conduction in different directions, resulting in regions with different strengths. Another byproduct of the working principle of AM is poor surface-finish which make the components prone to fatigue cracking. Although in some special cases it can be used to an advantage for increasing the performance in heat-convection of a component. Presence of some of these kinds of defects can lead to premature and abrupt failure of products.

In addition to that, the metal powders are not self-supporting, which creates the need for supports for overhang structures. This aspect constraints the design to an extent as the designer must reduce the number of supports needed for economical design, and hence make some compromises. This shortcoming, in addition to the poor surface finish of AM parts, requires an additional step of post-processing by traditional techniques depending on the specifications needed for the final product. It adds to the time and resources required.

2. CLASSIFICATION OF METAL AM TECHNIQUES

Generally, metal AM technologies are distinguished based on the physical shape of the raw material, the mechanism used for fusing the raw-material together or the method used for running the machines. Among the raw-material types depicted in Figure 1, powder and wire are the most used as the metals needed for AM processes are both easily available and cheaper to be obtained in these forms as compared to other types. To make a completely or partially end-usable product starting from metal-powder or wire, the AM technologies which are most widely adopted are Laser Beam Powder Bed Fusion, Electron Beam Powder Bed Fusion, Powder Laser Energy Deposition and Wire Laser Beam Energy Deposition.



Figure 1: Classification of Metal AM Technologies [10]

2.1 Laser Powder Bed Fusion (LPBF)

Laser Powder Bed fusion is also known as Selective Laser Melting (SLM) or Direct Metal Laser Sintering (DMLS). As the names suggest, it uses a focused laser beam to selectively melt metal-powder deposited on successive layers to create a 3-dimensional component.

The build chamber of a LPBF machine consists of a build-platform that has the possibility to translate vertically. On one side of this platform, there is a powder-feeder chamber which contains the raw material in powder form; on the other side there is a powder-collector chamber. The build-chamber is completely isolated from the outside environment which ensures that no impurities are introduced inside the part being produced. It is also filled with inert gas which is used to continuously regulate the oxygen-content inside the chamber which has to be less than

0.1% by volume. The inert gas also helps in carrying the gaseous smoke emitted when laser melts the powder, away from the laser-beam and it makes sure that smoke does not hinder it. The build volumes for LPBF machines range from 50 mm × 50 mm × 50 mm to 800 mm × 400 mm × 500 mm.

As it can be seen in the top-left portion of Figure 2, initially the build-platform is at its topmost position, while the platform in powder-feeder chamber is at its bottom-most. The build-platform shifts downward by a height equal to the desired layer-thickness, while the platform in the powder-feeder chamber shifts upward by the height which is necessary to fill the build platform up to its brim. The roller or recoating-blade transfers and spreads the powder from the powder-feeder chamber on to the build platform. If there is an excess of powder, it falls into the powder-collector chamber, as it can be seen in the top-center portion of Figure 2. Then the power-source, a laser for this kind of technology, selectively melts the powder (top-right of Figure 2). The diameter of laser beam focus-area is usually around 0.1 mm [11] and can be altered for some machines. As mentioned in Section 1.3, most LPBF systems use near-infrared lasers with a wavelength of 1064 nm. This is because the source of laser, a Neodymium-doped Yttrium Aluminum Garnet (Nd-YAG) crystal produces laser more efficiently than other options in the market, which are also more expensive. In the past few years, lasers with shorter wavelengths in the visible spectrum are being widely researched because of the higher absorptivity of those wavelengths for materials like copper, aluminum, silver and gold. Once the laser has selectively melted the regions of interest for a specific powder layer, the whole procedure repeats itself. At the end of the process, the obtained 3D components are surrounded by an excess of powder which is removed from the build chamber and can be reused after going through some recycling processes.

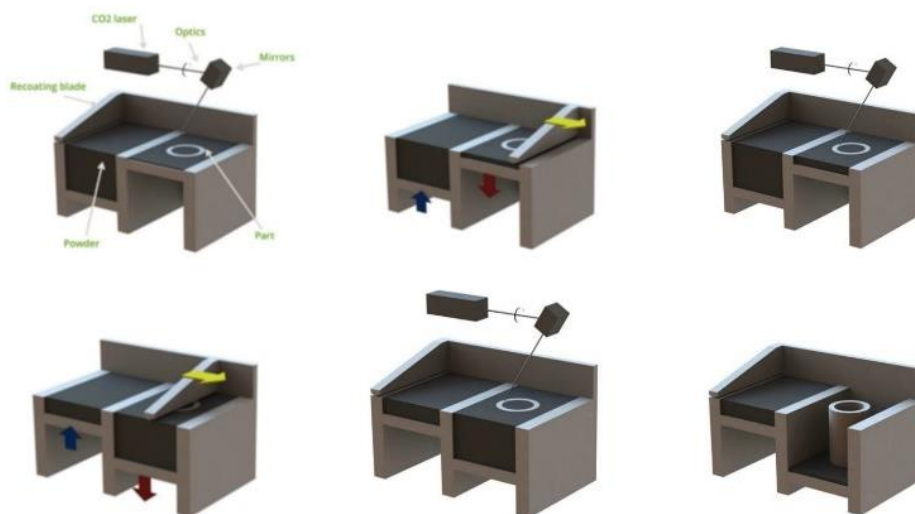


Figure 2: LPBF Working Principle

The newly produced part is generally heat treated, to relieve the thermal stresses that it endures during the process and some of the after-treatments like Hot Isostatic Pressing are also used to reduce any of the existing internal porosities. Most of the AM produced parts also need supports during the production. These supports are primarily used to avoid the distortion of overhang structures in the part, while also serving the purpose of heat dissipation during the manufacturing process.

The LPBF machine can be programmed so that the laser-beam follows a particular path. The different paths that the laser can follow are termed as ‘Scanning Strategies’. These different

strategies play a crucial role in the mechanical properties of the produced part. Generally, different strategies are distinguished by the different angles between the meandering parallel paths of 2 subsequent layers. It is common to adopt strategies with values of 90° or 67° for the aforementioned angular differences.

Along with scanning strategies there are 4 process parameters that can be varied for a LPBF system, which influence the state of the final product. They are:

- 1) Hatch distance (h_d): It is the distance between 2 adjacent, parallel paths of a laser. Varying this distance determines the percentage of remelting. If h_d is smaller than the melt-pool width, the melt-pools produced by adjacent laser paths will overlap and there will be remelting of solidified material; while if it is larger, they won't overlap and there is a probability of un-melted powder in the printed component. It generally ranges from 50 μm to 150 μm .
- 2) Scanning speed (v): It is the speed with which the focus-spot of laser traces the pre-defined path. Varying this speed alters the melt-pool dimensions. Deeper melt-pools are characteristic of slower speeds while shallower melt-pools are that of higher speeds. *EOS GmbH* is one of the leading manufacturers of LPBF systems, and the maximum scanning speeds that are achieved in their machines is 7 m/s [12]. Although, this speed is for repositioning the laser when it is not melting the powder. For melting, the speeds generally are in the range of 100 mm/s to 1 m/s.
- 3) Layer thickness (l_t): It is the distance by which the build-platform shifts down after every pass of the laser. Subsequently, new layer of powder is added on top of the platform. This parameter is also related to the remelting of powder. The depth of the melt-pool determines the percentage of remelting of the powder. Depending on the LPBF system, layer thickness can be varied from 10 μm to 100 μm .
- 4) Laser Power (P): It determines the amount of energy that is transferred from the laser to the powder per unit time. Currently, majority of the machines in the market have a laser power ranging from 100 W to 1000 W.

Different combinations of the above process parameters result in varying shapes and sizes of the melt-pools, which in turn affects the properties of the component. To find the right combination of parameters that yields the desired properties, initially a study of Single Scan Tracks (SSTs) is performed. In this study laser melts the powder in a straight line and multiple lines of powders called tracks are melted with different combination of parameters. The shape of the fused powder created by the SSTs varies depending on the Line Energy Density (LED). LED is given by:

$$LED = \frac{P}{v} \text{ (J/mm)}$$

Phenomenon known as 'Balling' is characteristic of lower LEDs whereas irregular lines or lines that are too thick can be seen for higher LEDs. Balling occurs when the size of the melt-pool is small in the XY plane so that subsequent melt-pools don't fuse together. The surface tension in the melted region prevents the fusion of the adjacent pools, causing individual spheres along the SSTs which increases the surface-roughness. This happens due to low power of the laser or too high scanning speed. On the other hand, thicker and irregular lines are observed as the higher LED creates deeper melt-pools due to a phenomenon called 'Key-hole melting'. In this regime a cloud

of metal-vapor is created at the location where the laser-powder interaction takes place. This cloud then settles on the surface and thickens the line of melted powder. It is not favorable to operate in this regime as excess power is consumed by it or more time is required to print a part due to low scanning speeds. It also modifies the composition of the component and pollutes the build-chamber. Optimum LED yields a uniform line with a smooth surface and optimum power consumption.

This study of LED by SSTs is extrapolated into Volumetric Energy Density (VED) for 3 dimensional components, by introducing the other degrees of freedom of hatch distance and layer thickness. Where the hatch distance is responsible for determining the amount of overlapping between adjacent melt-pools in XY plane, layer thickness is responsible for determining that amount in the build-direction. Higher overlapping consumes excess power and time, while lower overlapping introduces the possibility of pores in the microstructure and/or lack of fusion between adjacent melt-pools. It is given by the formula:

$$VED = \frac{P}{v \times h_d \times l_t} (J/mm^3) [13]$$

The major advantage of LPBF process over the other AM processes discussed subsequently is the higher surface quality. This is mainly due to the Particle Size Distribution (PSD) used. For Electron Beam melting (EBM) and Directed Energy Deposition (DED), the PSD ranges from 50 μm to 150 μm [14] [15], while for LPBF it generally falls in the range of 15 μm to 60 μm [16] [13]. This allows to obtain lower surface roughness of around 20 μm to 40 μm for LPBF parts, which is a large improvement. A good surface quality is important for the fatigue life of the component and aesthetic appearance. Although, the downside to having lower surface roughness, is lower heat transfer for heat exchanger applications [17]. The lower PSD allows for more intricate patterns to be created too, hence feature resolution is higher for LPBF machines.

The range of materials for LPBF is larger as well, because the material does not have to be conductive to be processable, which is the case for EBM. Polymers, metals and ceramics can be processed using LPBF, but only conductive-metals using EBM.

2.2 Electron Beam Powder Bed Fusion

Also known as Electron Beam Melting (EBM), it is a process whose fundamentals are similar to LPBF. The major difference is the power source which interacts with the powder. For LPBF it is a laser beam, whereas for EBM it is an electron beam.

The PSD for this process is generally higher than LPBF as mentioned in Section 2.1, because of the higher penetration depth of the electron beam. The build chamber is similar to a LPBF system with powder feeding mechanism and build-platform, although the build environment is vacuum in case of EBM. The vacuum prevents any oxidation of the powder during the process and it also avoids any interaction of the electron beam with particles. As it can be seen in Figure 3, there is a cathode at the top of the Electron Beam Column. A filament inside the cathode is heated to emit the electrons. The astigmatism lens (or the anode) makes the emitted electron beams parallel to

the electron beam column. Focus lens controls the thickness of the electron beam. The deflection lens is used to scan the surface of the powder-bed. This lens deflects the electron-beam using magnetic flux. As it has no moving parts, it is faster than the mechanically-driven deflectors of LPBF and also needs lesser maintenance. The scanning speeds for EBM machines can reach up to 8000 m/s [18].

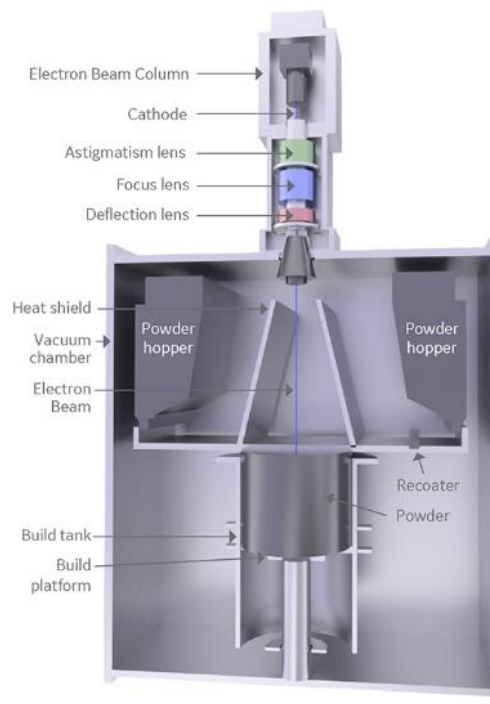


Figure 3: EBM working principle [19]

Before selectively melting the powder, the electron beam sinters all the exposed powder on the surface. As the powder is already at elevated temperature, there are minimal thermal stresses inside a component, avoiding the need for heat treatments. The higher temperature also means lower time for melting. The sintered powder also acts as supports for the component, carrying the heat away from it and facilitating the production of overhang structures and stacking of components.

One of the major drawbacks of EBM is the surface roughness. As the PSD used in EBM is higher than that of LPBF, the surface roughness is higher as well. The surface roughness increases the risk of fatigue failure for mechanically-loaded components produced with EBM. Another disadvantage of having a higher PSD is lower feature resolution of the components. The minimum thickness of walls is higher in case of EBM as compared to LPBF, affecting the design of lattice-structures. Sintering of powder introduces the need for post-processing, as the powder sticks together and cannot be removed manually. A powder removal station has to be deployed where the powder used for manufacturing is mixed with compressed air and sprayed on to the sintered cake using a hand-held gun. The portfolio of materials for EBM systems revolves only around conductive alloys of titanium, copper, nickel and cobalt-chrome.

2.3 Directed Energy Deposition

Also known as Direct Metal Deposition (DMD) or Laser Engineered Net Shaping (LENS). It has a working principle, almost identical to welding. Figure 4 shows the working of DED. A laser beam is focused on to the substrate. The substrate can be different depending on the purpose of using DED. It can be a metal-plate for building a new-component, or it can be a component which is to be repaired or coated. Due to its ease in repairing damaged parts, majority of applications of DED is in repairing-sector. The laser beam locally melts the substrate creating a melt-pool. This region of melt-pool is shielded with an inert gas, usually Argon, to prevent oxidation of the melted metal. Material is supplied to this region in the form of wire or powder causing the material-volume to increase. Once the laser moves away from the region it solidifies and a raised track is obtained. The deposition is controlled by the relative movement between the deposition head and the substrate. The deposition head creates tracks of deposited material. Several of these tracks when overlapped form a layer of material. After creating a layer, the deposition head moves ahead from the substrate by a distance equal to the layer thickness.

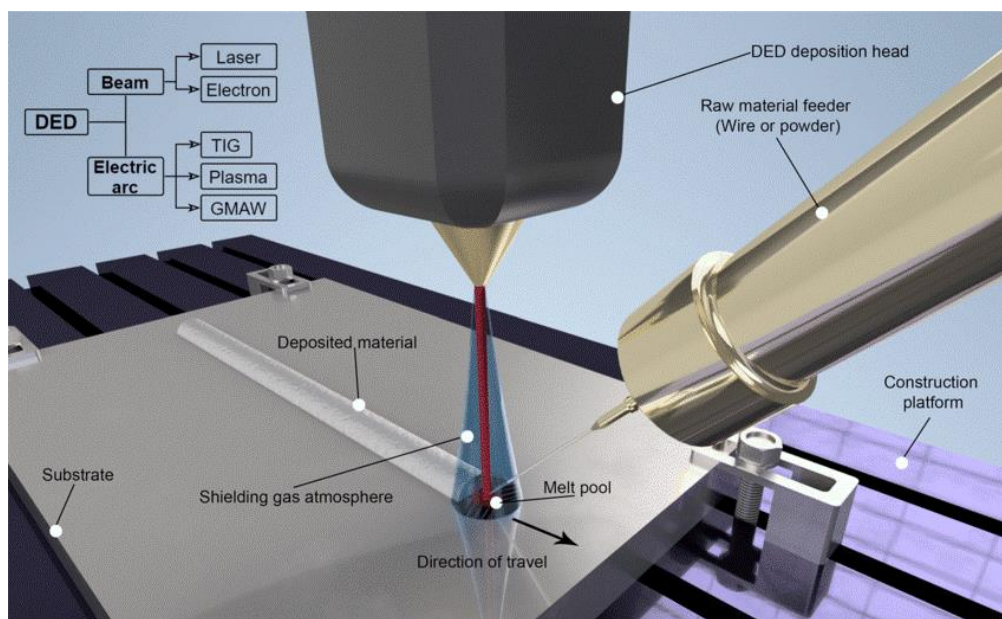


Figure 4: DED Working Principle [20]

One of the main advantages of this method are the wide variety of materials that can be used to create parts. Virtually all the metals that are ductile enough to be converted into a roll of wire or that can be turned into powder-form using atomization, can be used for DED. The build volumes are larger than LPBF or EBM systems as the size of the component is not restricted by the maximum travel of the build platform, but it is only restricted by that of the deposition head. The speed with which components can be fabricated is higher as well, because of the larger PSD used in case of powder-DED and the feed-wire used in case of wire-DED. The initial cost of the machine is also relatively low, as a conventional build-chamber is not present.

On the other hand, the main disadvantages would be the poor surface finish due to larger PSD of powder and also lower dimensional accuracy as a result of the poor surface finish.

3. COPPER AND ITS ALLOYS FOR AM

3.1 Copper and its alloys used for traditional manufacturing methods

The most extensive and exhaustive list of copper alloys and their segregation based on the alloying elements used, is published by *Unified Numbering System (UNS)*, which is an organization that was initiated by the *American National Standards Institute (ANSI)* in 1974 and is now administered jointly by *Society of Automotive Engineers (SAE)* and *American Society for Testing and Materials (ASTM)*. In the designation system wrought copper alloys are designated from C10000 to C79999, while cast alloys are designated from C80000 to C99999. The major groups of copper alloys are summarized in Table 1.

Table 1: UNS Copper and Copper Alloys families [21]

Copper Alloys	Description
Coppers	The copper content in these alloys is minimum 99.3%.
High Copper Alloys	<ul style="list-style-type: none"> Wrought alloys from this group have a copper content between 96% and 99.3%. Cast alloys from this group have more than 94% copper. Some of these alloys contain silver.
Brasses	<p>Zinc is the main alloying element for this group.</p> <ul style="list-style-type: none"> Wrought alloys have 3 main families of brasses: <ol style="list-style-type: none"> Copper-zinc alloys Copper-zinc-lead alloys Copper-zinc-tin alloys Cast alloys have 4 main families of brasses: <ol style="list-style-type: none"> Copper-tin-zinc alloys Manganese bronze alloys Copper-zinc-silicon alloys Copper-bismuth alloys
Bronzes	<ul style="list-style-type: none"> Wrought alloys have 4 main families of bronzes: <ol style="list-style-type: none"> Copper-tin-phosphorous alloys Copper-tin-phosphorous-lead alloys Copper-aluminum alloys Copper-silicon alloys Cast alloys have 4 main families of bronzes: <ol style="list-style-type: none"> Copper-tin alloys Copper-tin-lead alloys Copper-tin-nickel alloys Copper-aluminum alloys
Copper-nickels	Nickel is the main alloying element in this group
Copper-nickel-zinc alloys	Zinc and nickel are the main alloying elements in this group
Leaded coppers	Cast copper-alloys of this group have lead above 20%
Special alloys	All the alloys that are not included in the above groups are counted in this group

3.2 Copper Alloys currently used in AM

Copper is known for its high electrical conductivity of 58 MS/m, second only to silver [22]. Owing to this and its ductility, relatively higher availability, lower cost, its widely used for making electrical wires and in PCBs. It is lesser known for its equally important property of high thermal conductivity of 398 W/mK, again second only to silver [23]. This makes it popular for heat exchanger applications. These excellent physical properties of copper can be further enhanced with AM. This is because the characteristic surface-roughness of an AM part increases the heat transfer co-efficient further, the seamless parts without any assemblies increase the electrical conductivity of the part as a whole. Some applications of AM Copper, that are already being used in the industry are mentioned below:

- 1) Induction coils for hardening of gears: Induction hardening of gears improves substantially when coils made using AM are utilized. Traditionally, manufactured coils are braze-welded which does not produce uniform magnetic fields. Complex shapes of AM coils are smooth-enough to produce uniform magnetic fields.
- 2) Rocket engines: Traditional rocket-engine nozzles are manufactured using Inconel super-alloys which are robust for temperatures at which the combustion of fuel takes place inside it. Titanium alloys are also used alternatively. These materials although are superior in strength, they lag behind when it comes to thermal behavior of copper. A Brooklyn-based company called *Launcher*, used an AMCM M4K LPBF machine, with a build volume of 45 cm × 45 cm × 100 cm, to exploit the superior thermal properties of copper and apply it to rocket engines [24]. The nozzles of rocket-engines are basically heat exchangers, where the cryogenic propellants of hydrogen or oxygen are heated by the exhaust gases and this also keeps the body of the nozzle from melting away. By using AM Copper, the traditionally welded tubes that carry the propellants around the nozzle can be eliminated as inbuilt channels inside the nozzle can be manufactured in one piece. Moreover, the higher thermal conductivity of the material requires lower surface area for the same amount of heat to be transferred, resulting in weight reduction overall, which is paramount when it comes to the field of aerospace.
- 3) Antennae with mini-antennae: Antennae in electronic devices make use of AM of copper to obtain omni-directional properties. That can be obtained by having mini-antennae on the primary antenna, which can be conveniently manufactured using Copper AM.

The real-world examples mentioned above are just the tip of the iceberg. With the boom of AM and the predicted increase in adoption of AM over traditional techniques, the application field will get wider by the day. Although there are very important advantages of usage of copper for AM, it also has some major shortcomings that can stomp its growth if not addressed. Some of the prominent challenges faced when working with copper in AM are as follows:

- 1) Excellent conductor of heat: This strength of copper is its weakness as well, when it comes to PBF AM. As the power source, laser beam or electron beam, melts the material and creates a melt-pool, the material surrounding the pool transfer the heat away from it. As a result, to obtain a part without defects like porosities, lack of fusion or balling, the VED must be higher than when processing other materials. This means an increment in the already high power consumption of LPBF systems, a decrement in the other process

parameters of hatch spacing, layer thickness and scanning speed. This contributes in further increasing the production time and expenses.

- 2) Highly reflective: It's a challenge particularly for LPBF. Copper is highly reflective for laser beam in the infrared range, not as much for an electron beam. The absorptivity of pure copper for a wavelength of 1064 nm is less than 10% [25]. Although this absorptivity is for a bulk component. For a powder bed the absorptivity increases due to scattering of laser and internal reflections inside the powder bed and the absorptivity increases up to 30%, which is still a low value. The laser is reflected away from the powder-bed and can damage the unshielded components inside the build-chamber. It has been known to damage the optical instruments that guide the laser due to laser reflecting back to the optics [26]. This absorptivity further increases with decreasing powder-size and increasing alloying elements. There can also be temperature fluctuations inside the chamber which can lead to anisotropic physical properties of the manufactured product.

Copper alloys with high difference between solidus and liquidus temperatures undergo hot-cracking (solidification-cracking) during cooldown process. This makes Bronzes (From C50000 to C69999) and Nickel-Silvers alloys (From C73500 to C79999) (listed in Table 1) very difficult to be processed by LPBF. Nickel is completely soluble in copper for any proportion, which should make Copper-Nickels (From C70000 to C73499) a good candidate for LPBF processing. Although, due to the presence of unavoidable impurities of oxygen and sulphur in the powder, Copper-Nickels are embrittled after processing. They can develop hot-cracks as well [27]. On the other hand, Coppers, High Copper Alloys and Brasses are readily processable and does not develop hot cracking. For brasses (From C20000 to C49999), which are characterized by a significant amount of zinc, the thermal and electrical conductivities are affected and are about 1/3rd as compared to pure copper. This is the reason why these alloys do not have thermal or electrical applications; however, 3D printing for brass is predominantly used to make jewellery products, home décor products or prototypes for visual-aids. Coppers (From C10100 to C15999) have very low alloying content, and hence they retain the high thermal and electrical conductivity of pure copper.

Table 2: Copper alloys currently used in AM [26]

Composition, wt%	AM process reported(a)
Cu	LPBF, EB-PBF, DED, BJ
Cu-(0.4–1.2)Cr	LPBF
Cu-(0.5–1.2)Cr-(0.03–0.3)Zr	LPBF
Cu-(0.5–0.7)Cr-(0.02–0.05)Zr-(0.02–0.05)Ti	LPBF
Cu-0.5Cr	LPBF
Cu-(1.3–2.5)Cr	LPBF
Cu-(20–25)Cr	EB-PBF, LPBF
Cu-7.2Ni-1.8Si-1Cr	LPBF
Cu-2.4Ni-0.04Cr-0.7Si	LPBF
Cu-15Ni-8Sn	LPBF
Cu-4.1Zr-1.1B	LPBF
Cu-4Sn	LPBF
Cu-(10–15)Sn	LPBF
Cu-10Zn	LPBF
Cu-15Zn-2.8Si	LPBF
GRCop-84-Cu-6.5Cr-5.8Nb	LPBF, DED, EB-PBF
GRCop-42-Cu-3.3Cr-2.9Nb	LPBF
Cu-11.85Al-3.2Ni-3Mn	LPBF

LPBF machine manufacturing company, *EOS GmbH*, have these copper materials in their portfolio: Commercially Pure Copper (Copper content greater than 99.95%, From C10200 to C10850) and Pure Copper (Copper content of 99.6%, C15600) [28]. High Copper Alloys (From C16000 to C19999) have relatively higher tensile strengths as compared to coppers. For example, one of the High Copper Alloys from EOS's portfolio, CuCr1Zr (UNS designation C18150), has an Ultimate Tensile Strength of 340 MPa after heat treatment as opposed to the 220 MPa for Commercially Pure Copper. The absorptivity of High Copper Alloys at a wavelength of 1064 nm is also better with respect to pure copper, and this results in a porosity in the as-built component of about 0.5% as compared to the porosity of 5% in pure copper [28]. Another widely used High Copper Alloy is CuNi2SiCr (UNS designation C18000). The major disadvantages of using as-built High Copper Alloys, are the lower thermal and electrical conductivities. However, these disadvantages are generally overcome performing a heat treatment similar to T6. Another drawback is lower elongation at break, which can also be increased up to a certain extent after heat treatments. Pure coppers are generally used when the application is not subjected to major mechanical loads, and the conductivity of the component is more important than mechanical strength. For applications which are subjected to significant mechanical loads along with thermal or electrical loads a compromise is made and High Copper Alloys are generally selected.

3.2.1 CuNi2SiCr (C18000)

This is the alloy, whose properties are going to be discussed subsequently in this thesis. There isn't a significant amount of research that has been taken place on the production of components using CuNi2SiCr alloy by AM processes, especially with low-power LPBF systems, which makes it important to investigate its characteristics [28][30][31]. According to UNS [21], the composition of C18000 is as follows:

Table 3: CuNi2SiCr composition

Element	Copper	Nickel		Silicon		Chromium		Iron
Percent	Remainder	Min.	Max.	Min.	Max.	Min.	Max.	Max.
		1.8	3.0	0.4	0.8	0.1	0.8	0.15

Copper and nickel are completely solid soluble in all proportions. This alloy crystallizes in face centred cubic lattice structure [29]. As it can be seen from Figure 5, for lower percentages of nickel in copper, the solidus and liquid lines are relatively close together, thus preventing cracking of component during solidification, whereas for higher percentages the lines are farther apart allowing the hot-cracks to form easily.

The major advantage of this alloy over C18150 is that the former's absorptivity of the traditional near infrared laser, with a wavelength of 1064 nm, of a LPBF machine, is significantly higher than latter. This translates to lower porosities inside the component, and lower power-need of the laser itself. Conventionally, a manufactured component is subjected to solutionizing heat treatment, water-quenching and then ageing at 450°C for anywhere between an hour to tens of hours. But as the working temperatures of LPBF process are close to solutionizing temperatures, and the cooling rate after LPBF process is high, the steps of solutionizing and water quenching can be avoided. Direct ageing can be performed at around 450°C to obtain a good trade-off between properties. The end-result of these heat treatments is the precipitation of δ -Ni₂Si silicide particles

in α -Cu matrix, which block fatigue or deformation cracks [26]. The heat treatment done at SLM Solutions include solution annealing at 930°C for 15 minutes, followed by water quenching, and next aging at 540°C for 2 hours with subsequent cooling in air.

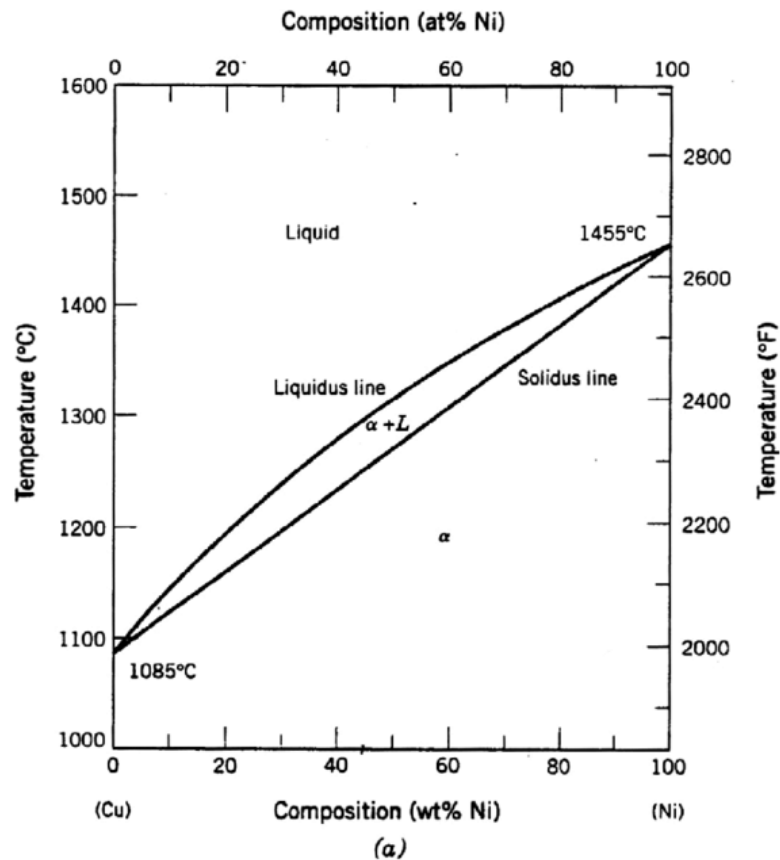


Figure 5: Copper-Nickel Phase diagram [30]

The microstructure consists of mostly columnar grains that are aligned with the building direction of the LPBF machine. The silicon presence in the alloy results in SiO_2 precipitates with a size of around a few nano meters. The oxidation of silicon maybe due to residual oxygen in the powder or its reaction with the environment. However, the presence of these oxides strengthens the component even further [26].

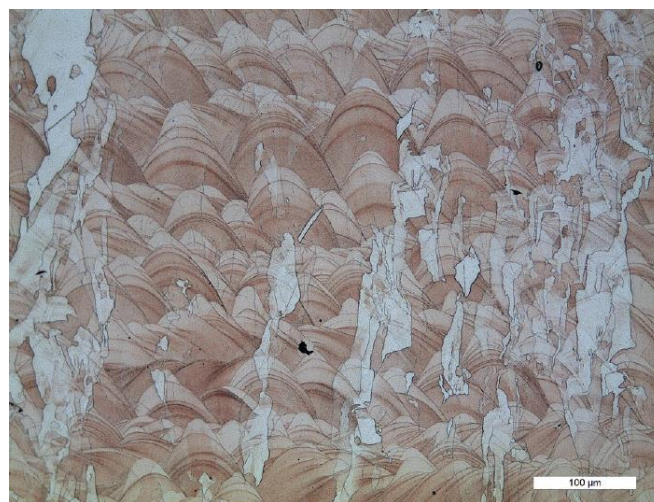


Figure 6: Microstructure of C18000 at 30X magnification [31]

The US-based company *Protolabs* which uses LPBF machines of Concept Laser from General Electric, provide their clients with an option to manufacture products using this C18000 alloy. The reported value of UTS is 496 MPa with an elongation at break of 23%. This moderately high value of UTS is also maintained for elevated temperatures [27]. Whereas for the company of *SLM Solutions*, the UTS value post-heat treatment is 674 MPa [29]. Due to the addition of nickel and silicon this alloy has high resistance to corrosion, especially to cracking due to stress-corrosion. As per *Protolabs*, density of more than 99.5% after heat treatments is obtainable with their services. The thermal and electrical conductivity values almost double from 90 W/mK to 165 W/mK and from 8 MS/m (14% IACS) to 15 MS/m (26% IACS) respectively, after heat treatment [32]. Although the values are still considerably lower than the thermal and electrical conductivity values for pure copper of 398 W/mK and 58 MS/m (100% IACS) respectively. This is the price paid to obtain the moderately high UTS.

4. EQUIPMENTS USED FOR CHARACTERISATION OF POWDER

4.1 Flowability measurement

Flowability of powders is one of the most important characterization parameters because PBF technology is based on the deposition of homogeneous layers of powdered material. It mainly depends on inter-particle friction. The main properties influencing the friction are shape, density, size of powder particles, surface area, roughness and chemical properties of the surface of powder particles. Smooth flowing powder is important for PBF processes, as powders with low flowability tend to produce porosities into the component, as inter-particle friction prevents the flow of individual particles into voids. The flowability is higher for spherical particles with respect to particles showing an irregular shape; this allows to obtain higher density and lower inter-particle Van der Waal's forces.

The Hall flowmeter is the most widely accepted method to determine flowability of a powder. The procedure to measure the flowability using Hall Flowmeter is defined in ASTM B213-13 [33] standard, which is as follows:

- 1) 50 grams of powder is taken in a container.
- 2) The powder is poured into funnel of Hall flowmeter (diameter of xx mm, while blocking the orifice at the bottom of funnel with a finger. It has to be made sure that the finger is dry.
- 3) Another container is placed at the bottom of funnel to collect the powder that falls from the cone.
- 4) The powder is allowed to flow freely into the container below funnel by removing the finger and thus unblocking the orifice. Time-measurement should start on a chronometer (having a least-count of at least 0.1 seconds) at the instant when the orifice is unblocked.
- 5) The time-measurement is stopped at the same instant when the last particle of powder falls into the container below the funnel

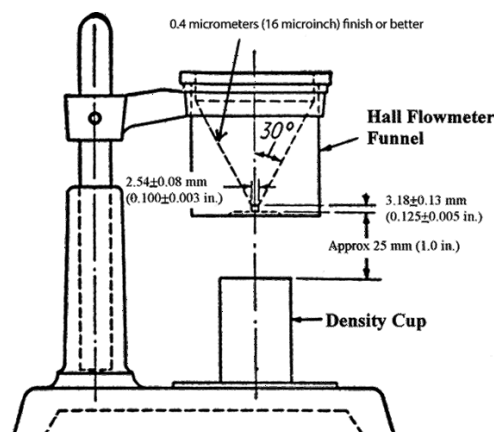


Figure 7: Hall Flowmeter Apparatus [34]

The procedure thus measures the time it takes for the 50 grams of powder to flow out of the funnel. During the procedure if powder stops flowing, it is allowed to tap the rim of funnel one time by striking it so that the powder continues to flow.

4.2 Density measurement

4.2.1 Tapped Density

Tapped Density is the density that the powder has after a process of compaction that allows particles to organize themselves to occupy a fixed volume as effectively as possible. The process to measure the quantity has been carried out in alignment with the described methods in the internationally accepted standard of ASTM B527-15, which is as follows:

- 1) A cylinder with a volume of 25 cm³ is cleaned with alcohol to eliminate the residues of previously used powders.
- 2) The cylinder is then filled with the powder, whose density is to be measured, up to the brim and excess powder is brushed-off from the brim.
- 3) The filled cylinder is then weighed and the weight of empty cylinder, that was previously measured, is subtracted from the weight of the filled-cylinder.
- 4) The system is mechanically agitated so that the powder inside the cylinder gets compacted and an empty space is created inside.
- 5) This empty space is refilled with new powder so that the powder level once again touches the brim of the cylinder.
- 6) The steps 4 and 5 are repeated until it is not possible to refill the cylinder with powder anymore and the filled cylinder is weighed again to obtain the final mass of powder.

The above steps are repeated thrice for different batches of powders, and the mean values of masses is calculated. The obtained values of masses are then used to calculate the Tapped Density (ρ_{tapped}) as follows:

$$\rho_{\text{tapped}} = \frac{m_{\text{tapped}}}{V}$$

Where, m_{tapped} : The average of masses of powder obtained at the end of Step 6 (grams)

V : Internal volume of the cylinder (cm³)

Another type of density, called 'Bulk Density' (ρ_{bulk}) is also calculated; it helps in further characterizing the powder. Its formula is as follows:

$$\rho_{\text{bulk}} = \frac{m_{\text{bulk}}}{V}$$

Where, m_{bulk} : The average of masses of powder obtained in Step 3 (grams)

V : Internal volume of the cylinder (cm³)

These 2 values of ρ_{tapped} and ρ_{bulk} are then used to calculate two parameters, 'Hausner Ratio' and 'Compressibility Index' as follows:

$$\text{Hausner Ratio} = \frac{\rho_{\text{tapped}}}{\rho_{\text{bulk}}}$$

$$\text{Compressibility Index} = \left(\frac{\rho_{\text{tapped}} - \rho_{\text{bulk}}}{\rho_{\text{tapped}}} \right) \times 100$$

The values obtained for Hausner Ratio and Compressibility Index, indicate the flowability of the powder as shown in Table 4.

Table 4: Flowability characteristics of powder [36]

Scale of Flowability		
Compressibility Index (%)	Flow Character	Hausner Ratio
< 10	Excellent	1.00 - 1.11
11 - 15	Good	1.12 - 1.18
16 - 20	Fair	1.19 - 1.25
21 - 25	Passable	1.26 - 1.34
26 - 31	Poor	1.35 - 1.45
3 - 37	Very poor	1.46 - 1.59
> 38	Very, very poor	> 1.60

4.2.2 Gas Pycnometer

Pycnometer is an extremely accurate instrument used to measure the density of an object with known mass i.e.; it measures the true volume of an object to obtain the true density (also called skeletal density). This instrument is especially useful in powder characterisation, as the procedure for finding 'Tapped Density' (discussed in section 4.2.1) doesn't take into account the empty volume between particles of powder when the value of 25 cm³ for the volume is input into the formula. The presence of porosities is another significant aspect that the previous method overlooks.

Commonly, gas-pycnometers are used more than liquid-pycnometers owing to the accuracy of the former type. This accuracy comes from the displacement medium used by gas-pycnometers, helium or nitrogen. The molecules of these gases reach the small pores which are inaccessible for liquid molecules of water. Another advantage is the nature of non-destructive testing of gas-pycnometers as the utilized gases are inert.

It uses the gas displacement method to measure volume of a bulk or powdered material. Generally, this method is more accurate and reproducible than the traditional Archimedes water displacement one. As shown in Figure 8, the sample is placed in the sample chamber whose volume (V_c) is known. The gas inlet valve is opened, and the chamber pressure is allowed to normalize. The expansion valve and vent valves are closed at this stage. Once the pressure is stable, the value is noted by the pressure transducer. The gas inlet valve is closed, and expansion valve is now opened. The gas is allowed to fill into the reference chamber, whose volume (V_A) is known. The pressure is noted again. The pressure ratio of the 2 noted pressures is then compared with the pressure ratio obtained during the calibration step of the instrument and using the ideal gas law equation the true volume of sample is calculated. For accurate application of ideal gas law equation, the temperature of the setup is monitored and kept constant. [35]

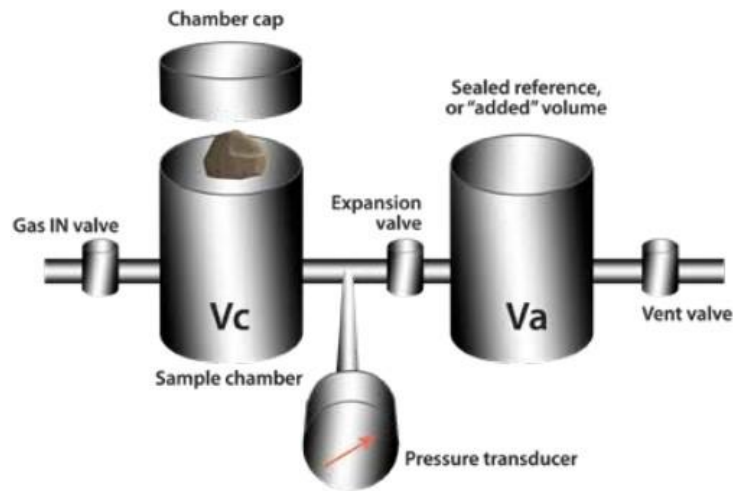


Figure 8: Gas Pycnometer Working Principle [35]

The density measurement for this thesis were performed using Anton Paar Pycnometer shown in Figure 9. This equipment was used to measure the density of both powder and printed bulk samples.



Figure 9: Anton Paar Pycnometer (Model: Ultrapyc 5000) [36]

4.3 Dimension measurement

The technique used to measure the Particle Size Distribution (PSD) of the procured powder is called Laser Diffraction Granulometry. PSD is one of the crucial parameters that influences the flowability of powder (as discussed in Section 4.1) and moreover the mechanical properties of the produced component. [37]

The working of this instrument is based on the 'Mie Scattering Theory' [38], which speculates that the angle of a diffracted beam with respect to the incident beam is smaller for larger particles

and vice-versa. As the powder is passed in front of the laser, the laser-beam diffracts in different directions depending on the powder size, position and its surface-morphology. These diffracted beams are detected by optical detectors as is evident from Figure 10. The intensity of the diffracted light and the pattern of detection across the detectors is fed into an algorithm which outputs the PSD of the powder. [39]

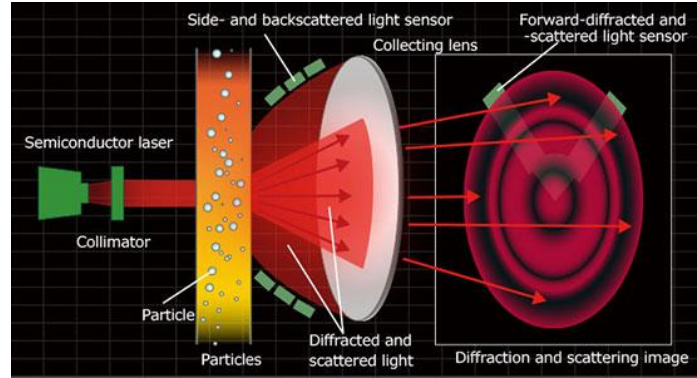


Figure 10: Laser Diffraction Granulometry Working Principle [40]

The equipment utilized for this purpose during the thesis was Malvern Panalytical's Mastersizer 3000, seen in Figure 11.



Figure 11: Granulometer Malvern Panalytical (Model: Mastersizer 3000) [41]

5. PRODUCTION OF TEST SAMPLES

The LPBF system used for producing samples of C18000 alloy was a machine procured from General Electric with the name 'Concept Laser Mlab R' (Figure 12). It uses a near-infrared (1070 nm) fibre laser (continuous wave) to selectively melt the powder with mechanism that is discussed in Section 2.1. Argon was used as the inert gas for the build chamber. The powder-portfolio for this machine includes steel alloys, titanium alloys, copper alloys, cobalt-chromium alloys, silver, gold and platinum.



Figure 12: Concept Laser Mlab LPBF system (Model: R) [42]

Following are its technical specifications:

Table 5: Concept Laser Mlab R - Technical Specifications [43]

Parameter	Data
Build envelope	90 mm × 90 mm × 80 mm
Layer thickness (l_t)	10 μm to 30 μm
Production speed	1 cm^3/h to 5 cm^3/h
Maximum laser power	100 W
Maximum scanning speed	7 m/s
Beam focus diameter	50 μm

Overall, 4 different batches of samples were produced. The laser-power for the machine was kept constant at 95 W, very close to the maximum value of 100 W. As discussed in Section 3.2, the use of IR laser for processing copper alloys through LPBF technology is very challenging because of the high conductivity and reflectivity of copper. Although research strategies generally use IR laser with high power to overcome these problems, this thesis tries processing a copper alloy by using a low power laser. A meandering scanning-strategy with laser-path rotated by 67° was used to try and achieve homogeneity inside the sample. The range of process parameters was chosen based on the literature research performed on copper and copper alloys in the AM field [44]–[51].

5. PRODUCTION OF TEST SAMPLES

Table 6: Jobs 1 and 2 process parameters

Job number	Sample number	Laser Power (W)	Scanning Speed (mm/s)	Hatch distance (mm)	Layer thickness (mm)
1	1	95	200	0.10	0.015
	2	95	180	0.10	0.015
	3	95	160	0.10	0.015
	4	95	140	0.10	0.015
	5	95	120	0.10	0.015
	6	95	250	0.08	0.015
	7	95	225	0.08	0.015
	8	95	200	0.08	0.015
	9	95	175	0.08	0.015
	10	95	150	0.08	0.015
2	1	95	200	0.10	0.010
	2	95	180	0.10	0.010
	3	95	160	0.10	0.010
	4	95	140	0.10	0.010
	5	95	120	0.10	0.010
	6	95	250	0.08	0.010
	7	95	225	0.08	0.010
	8	95	200	0.08	0.010
	9	95	175	0.08	0.010
	10	95	150	0.08	0.010

Table 6 reports the process parameters used for the fabrication of the first 2 series of samples (Jobs 1 and 2). Ten cubic samples were printed for each job with side 10 mm each. Job 1 was performed setting a layer thickness of 0.015 mm, while Job 2 was printed with a layer thickness of 0.010 mm. For these first 2 jobs, the process parameter of scanning-speed was varied from 120 mm/s to 250 mm/s; moreover, hatch distance (h_d) was also varied to find the optimum combination of the different process parameters that yield the highest relative density in samples. The printed samples attached to the build plate of the LPBF system can be seen in Figure 13 and Figure 14.



Figure 13: Job 1 printed samples with build-plate



Figure 14: Job 2 printed samples with build-plate

For Job 3, six cubic-samples of side 10 mm each were produced along with three dog-bone specimens to be used for tensile testing. The fabrication of cubic samples was performed by using the process parameters of the sample with highest relative density from Jobs 1 and 2. The printed samples with the build plate can be seen in Figure 15.



Figure 15: Job 3 printed samples with dog-bone tensile samples

For Job 4, different kind of samples were printed by using the same process parameters of Job 3. Four samples with a height of 10 mm were produced by progressively increasing the cross-sectional dimensions from 10 mm × 10 mm to 20 mm × 20 mm with a single-pass of the laser, as it can be seen in Figure 16. Along with them two additional cubic-samples of side 10 mm each with double-pass of the laser were produced as well. Moreover, two samples with dimensions of 60 mm × 6 mm × 10 mm were produced to be used for electrical conductivity tests. After printing these samples were cut into strips of 2 mm thickness each.



Figure 16: Job 4 printed samples

6. EQUIPMENTS USED FOR CHARACTERISATION OF TEST SAMPLES

6.1 Sample Cutting Machine

The machine that can be seen in Figure 17 was used to separate the produced test samples from the build-plate of the LPBF system. A cermet blade with constant water-supply for cooling it, was used to make the cut. The samples fixed to the build-plate is mounted on the cutting-bed using a clamp. The machine is equipped with a guiding-laser to accurately place the cutting-blade at the location where the cut must be made. The feed for cutting-bed can be set using the control panel of the machine along with the rotational speed of the blade. The feed and the rotational speed must be set in such a way that the maximum threshold of current absorbed by the machine (2.5 A) is not exceeded. As the material to be cut is a copper alloy, which is on the softer side, the feed can be set as high as 200 mm/minute. After the samples have been cut, any residual burrs on the sample cut-face are removed by manually polishing the cut-face using an 800-grit polishing paper.



Figure 17: QATM Precision Cut-off machine (Model: Brilliant 220) [52]



Figure 18: Sample cut-off from build-plate

6.2 Density measurement

The density of the printed bulk samples cut-off from the build plate, was measured using the Helium Pycnometer. The procedure of measurement was identical to that of density measurements of powder that has been explained in Section 4.2.2. The only difference was the change of a setting on the pycnometer, so that the machine understands that a bulk sample is being measured.

6.3 Metallographic compression mounting machine

The cut-samples are then placed inside the compression mounting machine where the samples are encapsulated into a resin. This procedure is performed as the dimensions of the sample are small, and manually holding the sample by-itself is not convenient for the next step of the process. A powdered resin is added into the chamber of the machine where the cut-sample is placed. The chamber-lid is then closed. The chamber is mechanically pressurized by a piston and the whole chamber is heated up to the temperature that is recommended by the resin manufacturer. The temperature of the chamber is regulated by the water supply to the machine. The elevated temperature is maintained for the time mentioned by the resin-supplier (155°C and 5 minutes respectively). Chamber is then depressurized, and temperature of the chamber is allowed to decrease until room-temperature. The encapsulated sample is then extracted from the machine.

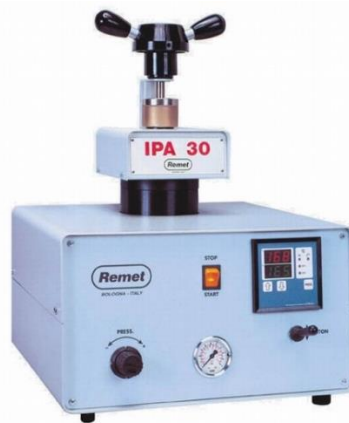


Figure 19: Remet compression mounting press (Model: IPA 30) [53]



Figure 20: Sample encapsulated in resin

6.4 Polishing machine

The polishing machine seen in Figure 21 was used to manually-remove the scratches on the desired surface of the test samples. It has a rotating platform whose speed of rotation can be altered. Polishing paper of different grits can be fixed to the platform. The head of the machine that holds the samples has a provision of rotation with different speeds as well. Although, the head was not used to polish the samples. A constant supply of water is available on the platform which washes away any loose particles and avoids heating of the sample surface.



Figure 21: Presi automatic polishing machine (Model: Mecatech 234) [54]

Following steps were followed during polishing:

- 1) Initially 800-grit paper was used to remove any burrs from the cutting process. The sample was held at the same orientation (with respect to the rotating plate) during the whole duration of polishing with this paper until all the scratches from the cutting process disappear from the surface.
- 2) The platform was cleaned with water to wash away any residual loose particles of metal, that can potentially scratch the surface during subsequent polishing steps. This step was performed between every change of polishing papers.
- 3) 2400-grit paper was used for the next step of polishing. During this step, the orientation of the surface of sample was rotated by 90° so that now the scratches from 800-grit paper are perpendicular to the rotation direction of the platform. The polishing with this paper was performed until the scratches from the previous step disappear.
- 4) The same process was followed for the next polishing paper of 4000-grit.
- 5) After 4000-grit polishing, the platform was fitted with a Rayon velvet polishing cloth. Colloidal silica solution with particle sizes of 6 μm , 3 μm and 1 μm was added continuously and slowly at the centre of the rotating cloth. Until a mirror-like surface is obtained with no visible scratches on the surface, the sample was polished.
- 6) The sample was then washed with soap and water carefully, and dried with a compressed air-gun.

6.5 Optical microscope (OM)

An inverted optical microscope that can be seen in Figure 22, was used to observe the microscopic properties of grains, melt-pools, porosities or cracks of the polished and etched samples. The microscope has a maximum magnification power up to 1000X. It is connected to a computer, which is used to operate the microscope in a more user-friendly way, and to save the images obtained on its hard drive.



Figure 22: Leica DMI Optical Microscope (Model: 5000M) [55]

6.5.1 Image analysis using *ImageJ* software

While one of the uses of the images acquired using OM is observing micro-structural properties, they can be utilized for evaluating the internal porosities of a sample, as well. Software *ImageJ* is used for this purpose. The software detects the contrast between the porous area and the non-porous one by detecting the difference in colours. The original image, as you can see from Figure 23, contains the porous areas as black-spots, while the light areas is where the metal-alloy is present.

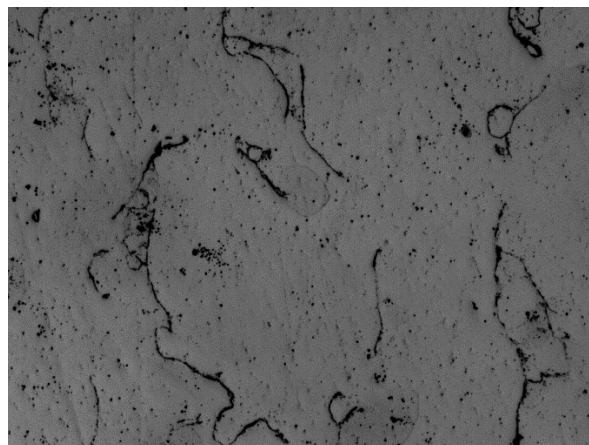


Figure 23: Image obtained from Optical Microscope

Importing the image into *ImageJ*, a threshold can be set based on the blackness of areas to be detected. This threshold value is a default value inside the software and is kept the same for all

the images processed using the software. The percentage of detected black areas is calculated by the software, as it can be seen below the histogram in Figure 24. This percentage is the porosity detected in that image.

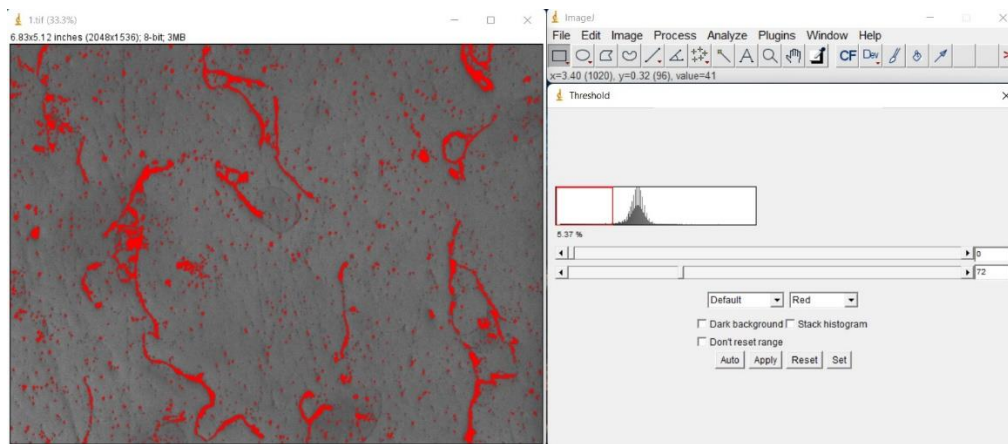


Figure 24: Setting threshold in ImageJ

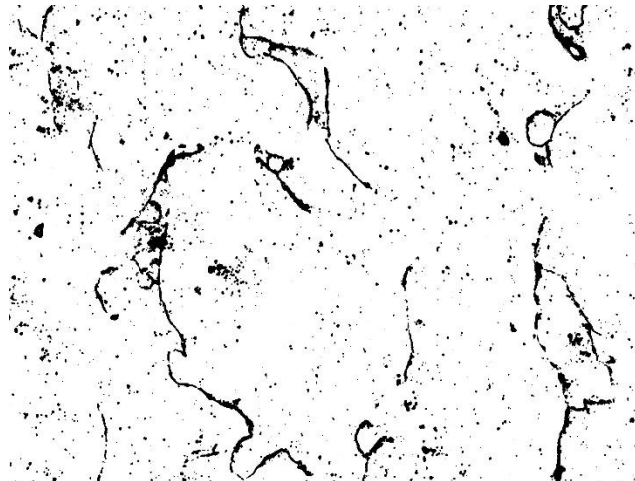


Figure 25: Detected porosity

As they are magnified images, the porosity calculated in such an analysis is a very localized property. For a more representational value of porosity for the sample, a number of images of different areas of the same surface of a sample were analysed using this software and the average of the values thus obtained was termed to be the porosity percentage in that sample.

6.6 Scanning Electron Microscope (SEM)

SEM is a highly sophisticated instrument that, similarly to an optical microscope, reveals the microstructure of a sample, however, it has a completely different working principle. A pictorial representation of the working-principle of SEM can be seen in Figure 26. It uses an electron beam instead of a light beam to produce an image of the surface under examination. The lower wavelength of the electron-beam as compared to light-waves produce images with higher resolution and hence SEM can achieve higher magnifications in the order of 100,000X. It operates

in vacuum thus preventing any interactions of particles inside the chamber with the electron-beam. It has a much higher depth of field, allowing for much more of the sample to be in focus, thus preventing blurry images in case of slightly inclined surfaces. These distinguishing features produce higher resolution images as compared to OM images.

The electron beam is emitted by the electron-gun which acts as the cathode of the instrument. The beams are oriented outwards from the point-source of the emitter. To change the direction of the beams so that they are parallel to each other and vertical, an anode is placed below the emitter. A magnetic lens is used to control the thickness of the electron-beam column, which determines the resolution of the produced-image. It also focuses the beams onto the sample surface. The scanning coils are used to move the electron-beam focus-point on different areas of the surface of the sample under observation. When the electron-beam impacts the surface of sample, different types of electrons and X-rays are emitted from the sample. The types of electrons that are used for imaging are back-scattered electrons (BSEs) and secondary electrons (SEs). While BSEs originate from deeper areas in the sample, SEs originate on the surface of the sample. Hence, BSEs and SEs contain different types of information which is interpreted by the SEM algorithm.

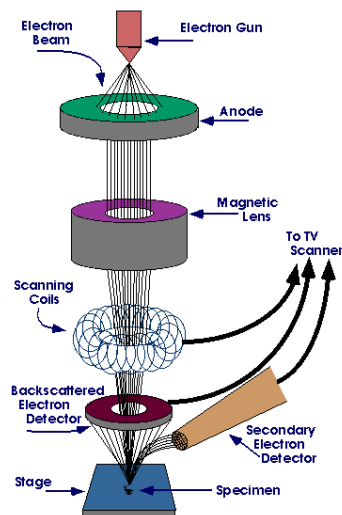


Figure 26: Working principle of SEM [56]

The SEM used for research purposes of this thesis is shown in Figure 27.



Figure 27: Alfatest Scanning Electron Microscope (Model: Phenom XL G2) [57]

6.6.1 Energy Dispersive X-ray Spectroscopy (EDS or EDX)

EDS analysis is performed to investigate the presence of different elements in the sample. It is a semi-quantitative as well as qualitative analysis, which means the results of the analysis not only shows the elements present in the sample but also shows the proportion of elements. The detector for conducting this analysis is usually furnished with an SEM or many SEMs have the provision to integrate it after their procurement as well.

As discussed in Section 6.6, when the primary electron beam impacts the sample-surface various types of electrons and X-rays are emitted from the sample. The X-rays that are emitted are characteristic of the elements they are emitted from. These X-rays are emitted because when the primary electron-beam displaces an electron from one of the core shells of the atom of an element, there is a void that is created in the shell. This void is filled by an electron in one of the outer shells of the atom. In doing so, the electron has to emit some energy as it is shifting from a high energy position to that of a low one. The energy emitted is in the form of X-rays and the intensity of those X-rays detected by the X-ray detector is interpreted by the system, which leads to the result of EDS analysis that ascertains the presence and proportion of elements.

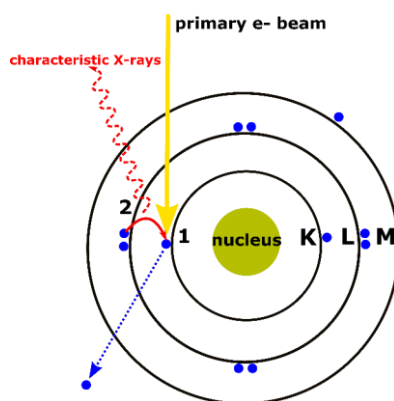


Figure 28: EDS working principle [58]

6.7 X-Ray Diffractometry (XRD)

XRD is mainly used to determine the phases present inside a crystalline material. The working principle of XRD is based on the Bragg's law of X-ray diffraction. Figure 29 gives an overview of the law. Crystalline solids create constructive or destructive interference patterns when X-rays are incident upon them at a certain angle. The pattern depends on the distance between 2 lattice planes and their orientation with respect to each other. If the path difference between the wave is a multiple of 2π the interference is constructive, while if it is π , the interference is destructive. Scanning through the 2θ angles for a sample and plotting the angles against the intensity of X-rays detected, creates a graph. This graph can be compared with a database of graphs to find the closest fit, which indicates the phase that is present inside the tested sample.

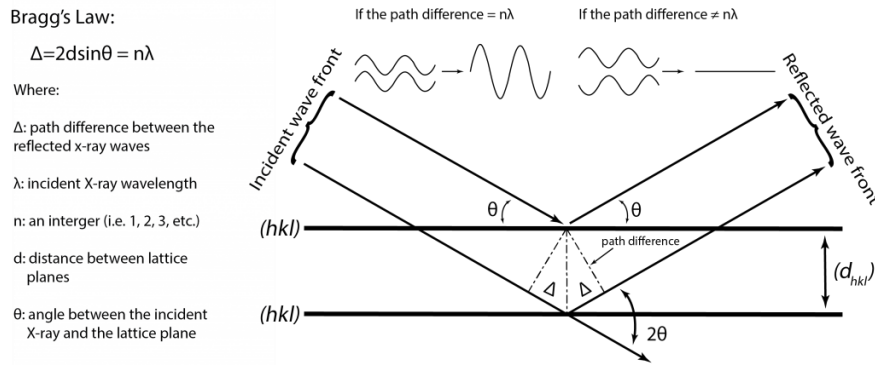


Figure 29: XRD working principle [59]

The XRD machine used for the purposes of research for this thesis is shown in Figure 30.



Figure 30: X-ray diffractometer from Malvern Panalytical (Model: Empyrean) [60]

6.8 Vickers Hardness Tester

The hardness of a material is described as its resistance to a permanent deformation under a static load. Vickers hardness tester is a versatile system as the hardness value is independent of the size of the indenter and any kind of material can be tested as the tester is equipped with a diamond indenter. The way it works is a known force is applied with the diamond indenter on the surface of the sample to be tested. As the indenter is a square-pyramid shape, the shape is indented on to the surface, which can be seen in Figure 31. The diagonals of this square are measured using an optical microscope.

The Vickers hardness number (HV) is calculated using the following formula:

$$HV = \frac{0.1891 \times F}{d^2}$$

Where, F is the force applied through the indenter (N)

d is the average of the measured diagonals of d_1 and d_2 (mm)

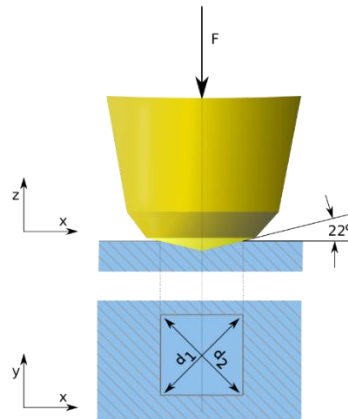


Figure 31: Vickers Hardness Test working [61]

The tester that was used was the DHV-100 Micro-vickers Hardness Durometer seen in Figure 32, to apply a force of 100 gF (0.98 N) for 10 seconds. 10 separate measurements were recorded.



Figure 32: Micro-vickers Hardness Tester from Chongqing Scope Instruments (Model: DHV-1000) [62]

6.9 Universal Testing Machine (UTM)

An UTM is a machine used for tensile, compression and flexural tests of a component. Properties such as yield strength, ultimate tensile strength and young's modulus can be evaluated using these tests. The tensile tests of the dog-bone samples shown in Figure 15 were performed using this machine. For the dimensions of the samples and the test parameters the ASTM E8M standard was followed, which is commonly applied for tensile tests of metals. The machine used for the test was Zwick Z100 that can be seen in Figure 33. Essentially, 2 methods of tests can be performed to evaluate the physical properties:

- 1) Strain-rate control : Where the strain-rate of the sample is kept constant
- 2) Load-control : Where the load on the sample is kept constant

The first method is widely adopted for its repeatability of results. Hence even for this thesis the first method was adopted.



Figure 33: Zwick Roell UTM (Model: Z100) [63]

6.10 Electrical Conductivity test

The 4-point probe method was used to determine the electrical conductivity of the samples. 4 parallel pins are used for the measurement as it can be seen in Figure 34. The inner 2 pins are used to measure the resistance with an ohm-meter, while the outer 2 pins are applied with a potential difference. The resistance (R) between the 2 inner pins is measured in ohms. The distance (l) between the 2 pins is known in mm. The cross-sectional area (A) is known in mm^2 . Hence electrical conductivity (σ) is calculated as:

$$\sigma = \frac{l}{R \times A} \text{ (S/m)}$$

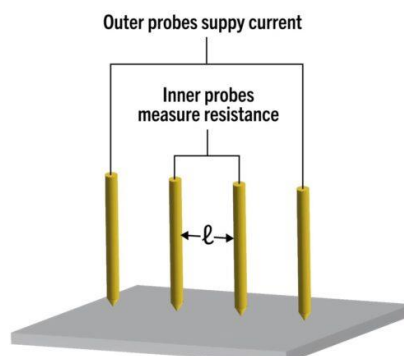


Figure 34: 4-point electrical conductivity test [64]

7. RESULTS AND DISCUSSION

7.1 Powder Characterization

The gas-atomized powder for the alloy of CuNi₂SiCr (C18000) was procured from *Praxair Surface Technologies*, a company from Indianapolis, the U.S.A. The powder is sold under the name Cu-175 by the company. The elemental composition of the alloy as provided in the datasheet of *Praxair Surface Technologies* is reported in Table 7, along with the values reported in the UNS Standard for the alloy. The values are reported in weight percentage. They are in acceptable limits.

Table 7: CuNi₂SiCr composition as per datasheet provided by *Praxair Surface Technologies*

Element	Copper	Nickel		Silicon		Chromium		Iron
UNS Standard (%)	Remainder	Min.	Max.	Min.	Max.	Min.	Max.	Max.
		1.80	3.00	0.40	0.80	0.10	0.80	0.15
Datasheet (%)	Remainder	2.61		0.51		0.45		0.08

The oxygen content in the powder determined by LECO Analysis was 0.050% by weight. This analysis was performed in July 2021 at the *Praxair Test Laboratory* before the batch of powder was shipped to *Politecnico di Torino, Italy*, where the research for this thesis was conducted. The LECO analysis was repeated twice in *Politecnico di Torino*, once in September 2021 and once in February 2022. For each analysis, 3 separate batches of the powder were tested. The weight percentage of oxygen obtained from these tests were 0.069 ± 0.002 % and 0.073 ± 0.001 % respectively; this suggests that the oxidation of the powder is negligible when it is stored, even for long durations of time.

The procured powder was observed under the SEM to determine the shape and the morphology of the individual powder particles. As it can be seen in Figure 35 a) and b), the particles are mostly spherical in shape with satellites attached to them. Satellites are smaller particles that get attached to larger particles during the process of atomization. Some other defects that are observable in Figure 35 c) are splat caps and agglomerations, which render the surface of the particles rough, making it difficult for the powder to flow freely. Figure 35 d) shows the grains and grain boundaries that constitute a powder-particle.

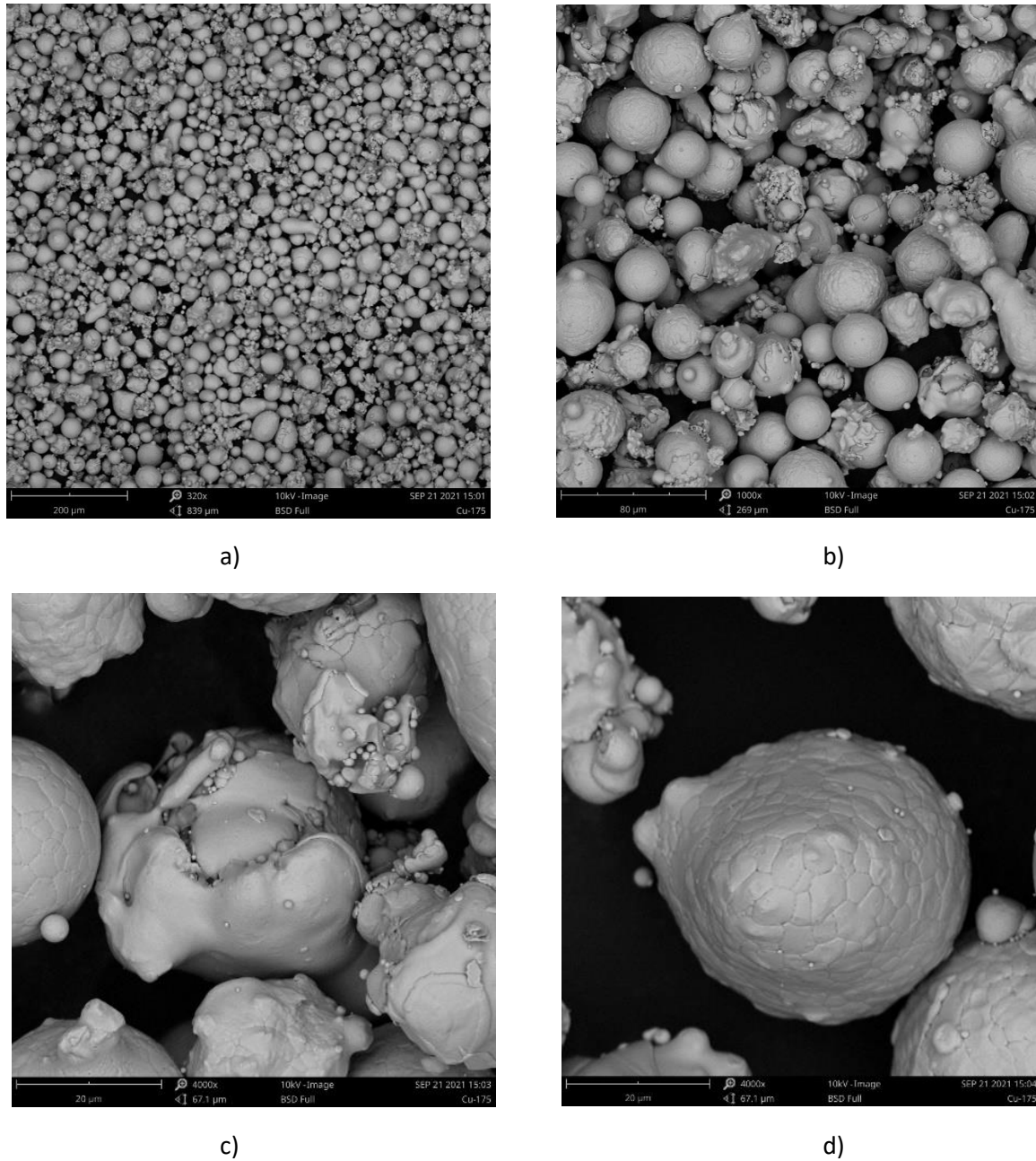


Figure 35: SEM images of procured powder

7.1.1 Flowability

The flowability of the powder was measured by the supplier and was reported to be 14.0 seconds/50 grams. It was measured according to the Hall Flow method discussed in Section 4.1. The same test procedure was also carried out at *Politecnico di Torino* for 3 separate samples of the same batch of the powder. The results corroborated the tests carried out by the supplier, by returning the values of 14.0 ± 0.2 seconds/50 grams.

7.1.2 Density

With the procedure explained in Section 4.2.1, the bulk density and tapped density values for the powder were calculated. They are reported in Table 8.

Table 8: Bulk and Tapped Density of Powder

Density	Value (g/cm ³)	
	Obtained	Datasheet
Bulk (ρ_{bulk})	4.72 ± 0.05	4.55
Tapped (ρ_{tapped})	5.36 ± 0.08	-

The obtained values of density were then used to calculate the Compressibility Index and the Hausner ratio as mentioned in Section 4.2.1. They are reported in Table 9. The averages of the values are within the threshold of excellent flow character, although the upper limits considering the variation of values suggest a good flow character.

Table 9: Compressibility Index and Hausner Ratio of powder

Parameter	Value	Flow character
Compressibility Index	8.94 ± 1.41 %	Excellent
Hausner Ratio	1.10 ± 0.02	Excellent

To find the real density of the powder-particles gas-pycnometer method explained in Section 4.2.2 was implemented. Three separate portions of the same batch of powder were tested in the pycnometer to obtain the value of 8.89 ± 0.02 g/cm³. The average value of 8.89 g/cm³ was used for the subsequent calculations of relative densities.

The relative density of powder-particles was calculated using the image analysis method explained in Section 6.5.1. Powder-particles were encapsulated in a resin with the same procedure that is explained in Section 6.3 and the bottom surface is polished following the procedure in Section 6.4. Then, a set of 15 images were taken with OM and imported into ImageJ software for finding the percentage of porosity, and hence the relative density. The black background of the resin can be eliminated in the software. The relative density value for powder thus obtained was 99.12 ± 0.22 %.

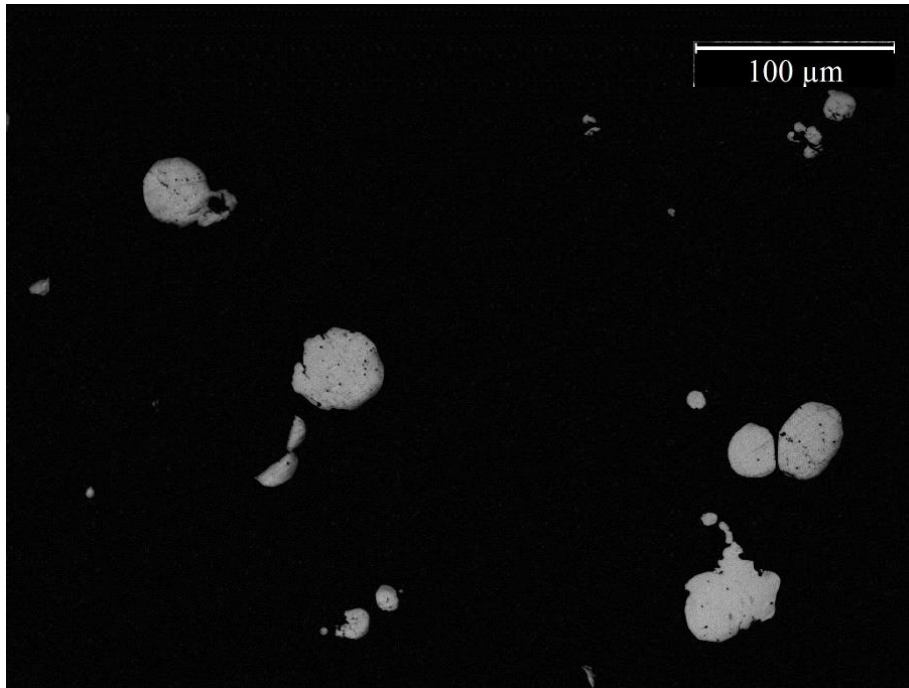


Figure 36: OM image of encapsulated powder (Magnification: 200X)

7.1.3 Particle size distribution

Particle Size Distribution (PSD) obtained using a Laser Diffraction Granulometry, (explained in Section 4.3), is reported in the Table 10 and the graph is depicted in Figure 37. The dimensions of the powder are acceptable to be processed in LPBF machine.

Table 10: PSD of powder

Diameter Percentile	d10	d50	d90
Diameter (μm)	19.7	31.4	48.8

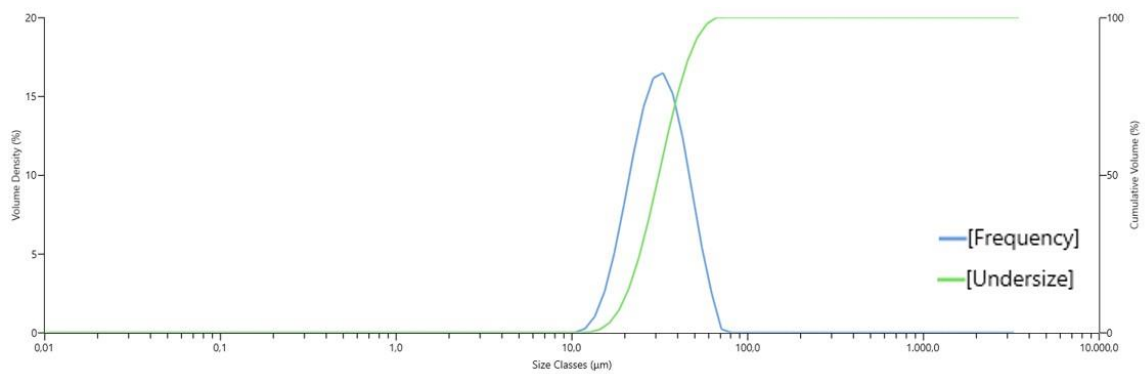


Figure 37: PSD of procured powder

7.2 Test Samples Characterisation

7.2.1 Relative Density

7.2.1.1 Jobs 1 and 2

The relative densities of the printed test samples were analysed using gas-pycnometer. As discussed in Section 5, Jobs 1 and 2 were performed to optimize the process parameters. The relative densities of all the 20 samples are plotted against scanning speed and VED in the graphs in Figure 38 and Figure 39. The highest relative density of 96.75% was achieved for sample number 8 of Job 1. The process parameters for that specific sample are mentioned in Table 11.

Table 11: Process parameters of the sample with highest relative density

Parameter	Data
Layer thickness (l_t)	0.015 mm
Hatching distance (h_d)	0.080 mm
Laser power (P)	95 W
Scanning speed (v)	200 mm/s

The second highest relative density is obtained for Sample 6 of Job 2, with a value of 96.09% which is not significantly lower with respect to the previously mentioned result. It is a good candidate for optimum parameters as well. However, considering that printing-times for parts with higher layer thicknesses are lower, the process parameters used for the fabrication of Sample 8-Job 1 are chosen to be used for subsequent jobs.

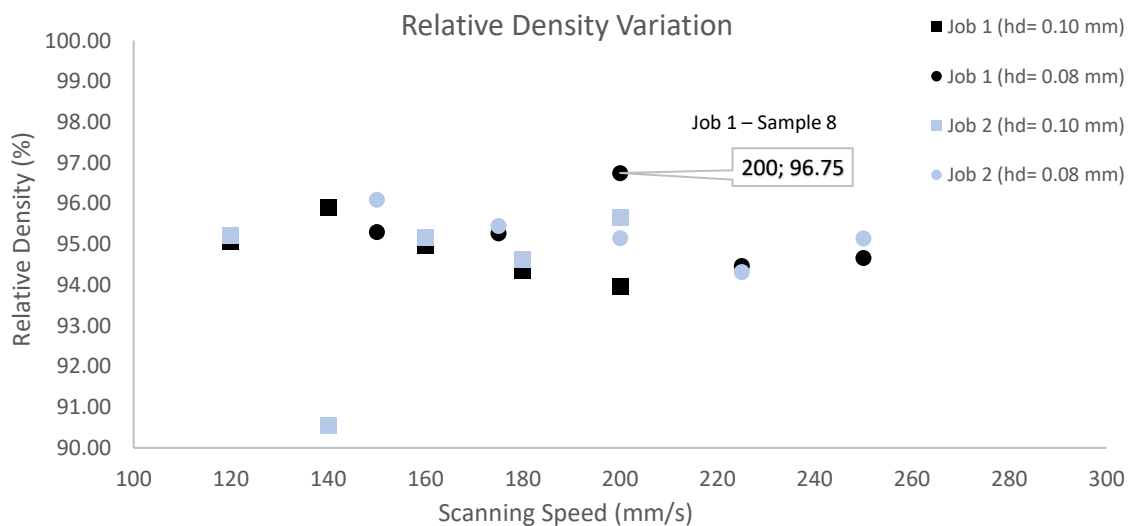


Figure 38: Relative density variation with Scanning speed

Figure 39 shows a slight trend where the relative density is increasing with the increasing VED. VED could have been further increased to corroborate this trend but considering the limited

maximum power of 100 W for the equipment, and non-feasibility of decreasing the process parameters of hatching distance, scanning speed and layer thickness due to time-constraints and/or machine constraints, VED couldn't be increased more than 800 J/mm³.

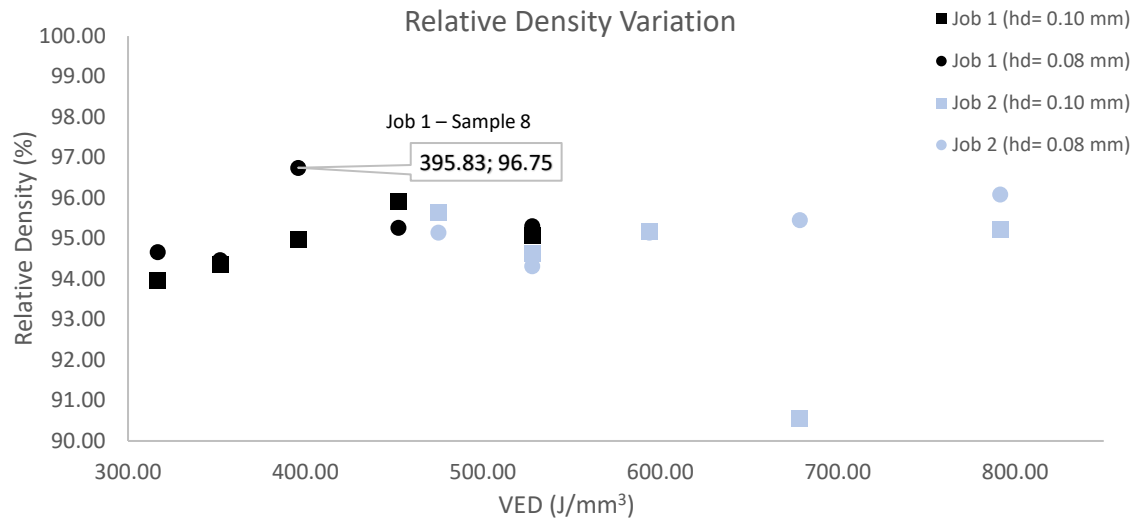


Figure 39: Relative density variation with Volumetric Energy Density

Graphs with different combination of parameters, were plotted to spot a trend in relative density variation. Although there was a slight trend with values of relative density peaking at a certain point and dropping-off on either side of the peak, the trend was not so pronounced to come to a definitive conclusion.

7.2.1.2 Job 3

The samples of Job 3 were printed using the process parameters optimized in Jobs 1 and 2. The relative density calculation of the samples in Job 3 verified the effectiveness of the selected process-parameters of Job 1-Sample 8. The average value of relative densities for all the 6 cubic-samples printed in Job 3 was 97.65 ± 0.73 %, with all the values more than the relative density value of Job1-Sample 8 of 96.75%, as it can be seen in Figure 40. This confirms the reproducibility of the process parameters.

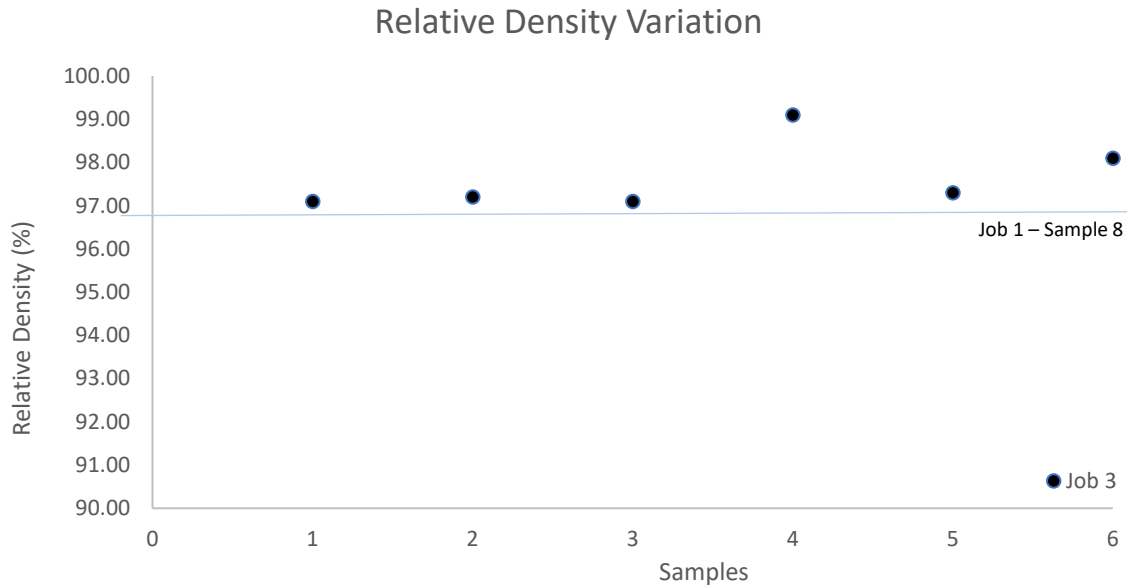


Figure 40: Relative density variation for Job 3

7.2.1.3 Job 4

In Job 4, as mentioned before, the possibility of increasing the relative density was investigated by increasing the number of passes of laser and by increasing the dimensions of the samples.

The strategy involving double-pass of laser yielded ineffective results as the relative density of the 2 samples produced in such a way had values of 96.92% and 96.80% respectively, which are very close to the value of relative density of samples with same dimensions but built using a single-pass strategy (96.98%).

On the other hand, the strategy of increasing the dimensions of samples in XY plane showed definitive trend of increasing relative density, as is clearly visible in Figure 41. A hypothesis could be, that the duration for which heat is supplied to the internal areas of a sample during manufacturing, increases with increasing dimensions. For highly conductive material like copper, it can be advantageous as it may result in higher temperatures in the interior regions and thus could play a role in decreasing the porosity. However, this hypothesis needs to be verified in the subsequent research projects.

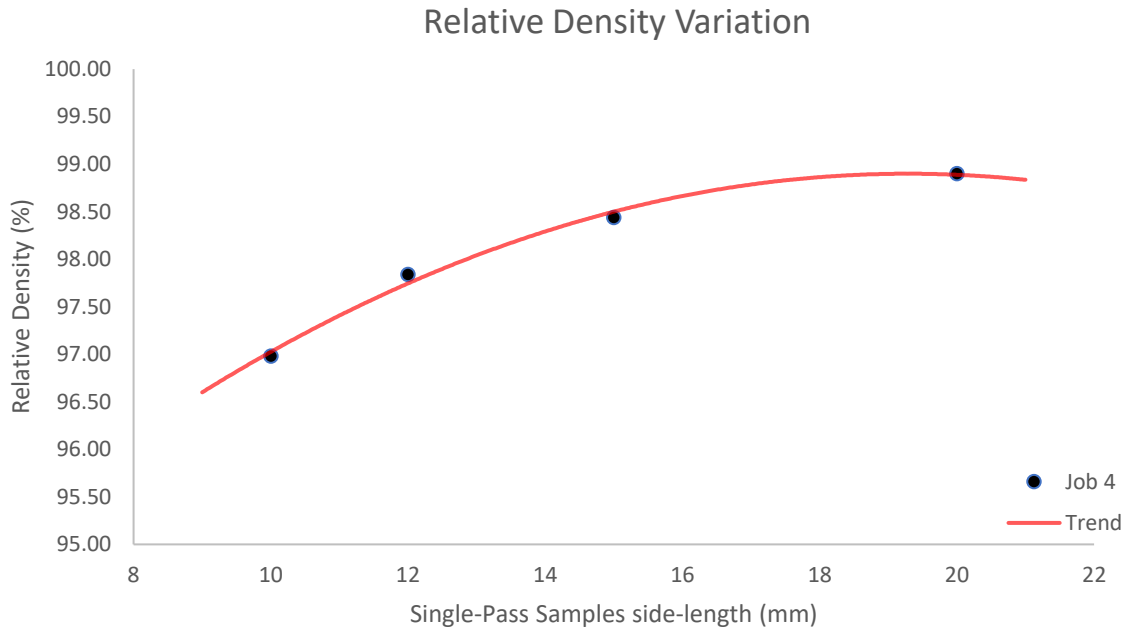


Figure 41: Relative density variation in Job 4 samples with single-pass of laser

7.2.2 Microstructure

7.2.2.1 Porosity comparison of samples

Samples with the highest and lowest relative density values for Job 1 and the sample with the highest relative density value from Job 3 were polished using the procedure mentioned in Section 6.4. The images taken by the optical microscope were analysed using *ImageJ* software, in a similar way which is explained in Section 6.5.1 to obtain Figure 25. This was used for verifying the relative density values obtained by pycnometer (mentioned in Section 7.2.1).

The images analysed with *ImageJ* show a lower relative density than the values obtained from pycnometer, as is evident from the examples shown in Figure 42, Figure 43 and Figure 44.

Relative Density: 93.96% (Pycnometer); 93.08% (ImageJ)

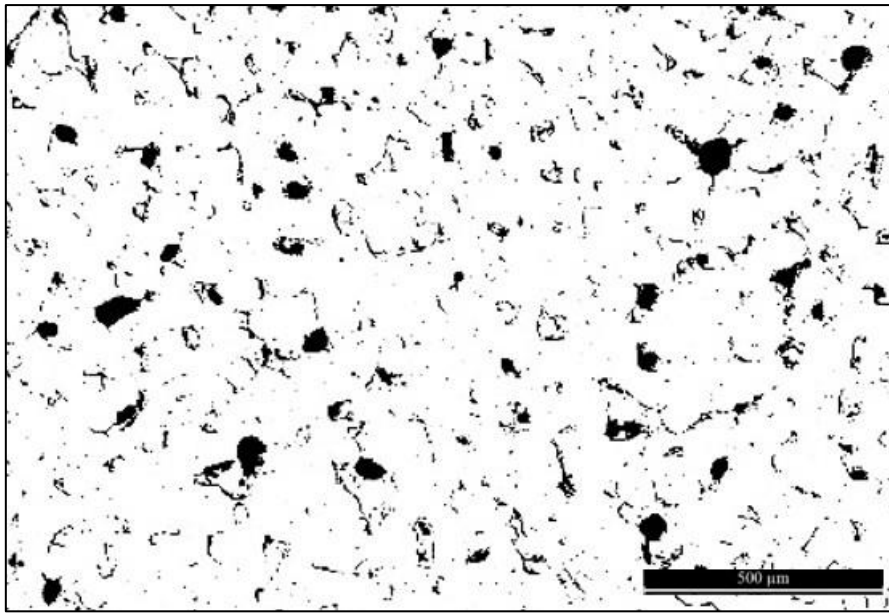


Figure 42: Job 1-Sample 1 OM image analysed with ImageJ software (Magnification: 50X)

Relative Density: 96.75% (Pycnometer); 96.29% (ImageJ)

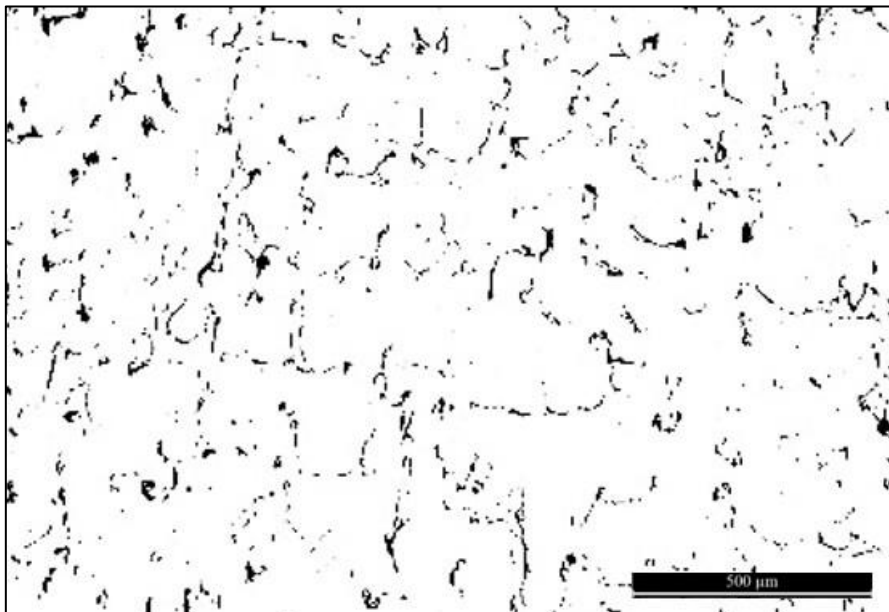


Figure 43: Job 1-Sample 8 OM image analysed with ImageJ software (Magnification: 50X)

Relative Density: 99.10% (Pycnometer); 96.97% (ImageJ)

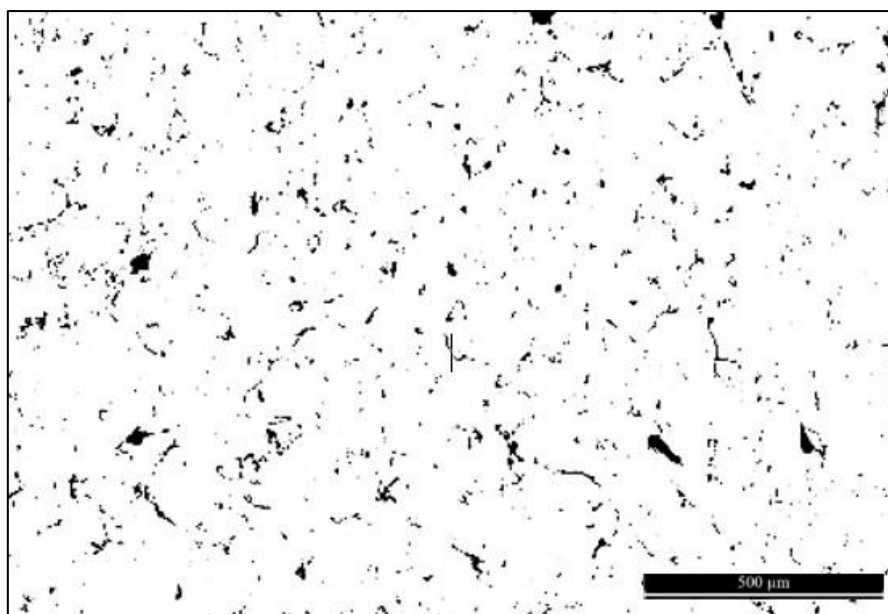


Figure 44: Job 3-Sample "D" OM image analysed with ImageJ software (Magnification: 50X)

To investigate this issue EDS analysis of the images was performed. The analysis revealed the presence of silicon in the black-spots previously assumed to be porosity. As it can be seen in Figure 45 and Table 12, the map analysis suggests that copper and nickel are in solid solution, whereas silicon is detected in the black spots without the presence of oxygen. Whereas it is evident in Figure 46 and Table 13 that there is a presence of oxygen along with silicon in the cracks. This suggests silicon oxides along with other oxides in the cracks and silicon in the black spots. The EDS spot analysis further confirms the presence of pure-silicon in the black-spots. The quantity of spots of silicon in the micro-structure is too large enough for them to be precipitates of silicon, originating from the silicon in the powder. As the percentage by weight of silicon in the procured powder is only 0.51%. This suggests an external source of silicon. The 2400 grade and 4000 grade polishing paper used are manufactured from Silicon Carbide. EDS analysis doesn't always detect carbon owing to the lower number of electrons in its outer shell, which is the reason carbon doesn't seem to be present in the EDS analysis map and spot analysis. It can be deduced that the black spots with irregular shape (not spherical) are not porosity, but Silicon Carbide chips originating from polishing paper which are getting embedded into the malleable surface of copper alloy. It also explains the lower relative density in case of *ImageJ* analysis.

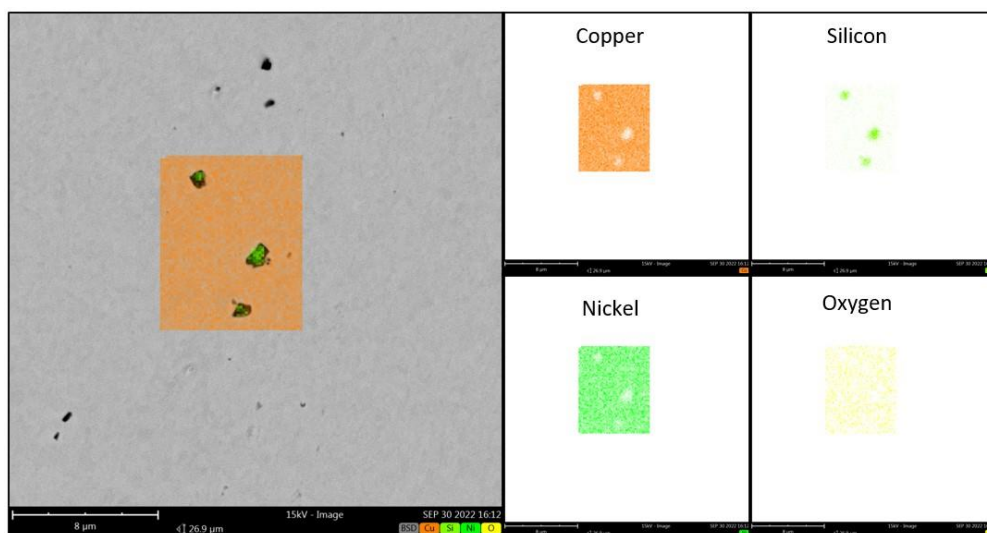


Figure 45: EDS Map Analysis

Table 12: Element concentrations inside map of Figure 45

Element	Atomic concentration (%)	Weight concentration (%)
Copper	92.14	95.19
Silicon	5.41	2.47
Nickel	2.45	2.34
Oxygen	0.00	0.00

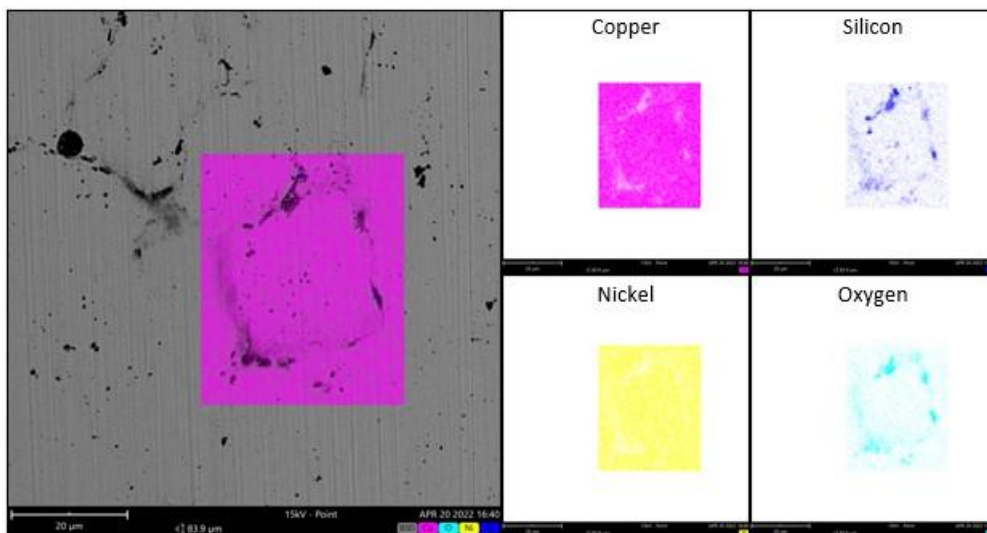


Figure 46: EDS Map Analysis

Table 13: Element Concentrations inside map of Figure 46

Element	Atomic concentration (%)	Weight concentration (%)
Copper	80.95	91.84
Silicon	4.34	2.18
Nickel	2.34	2.45
Oxygen	12.37	3.53

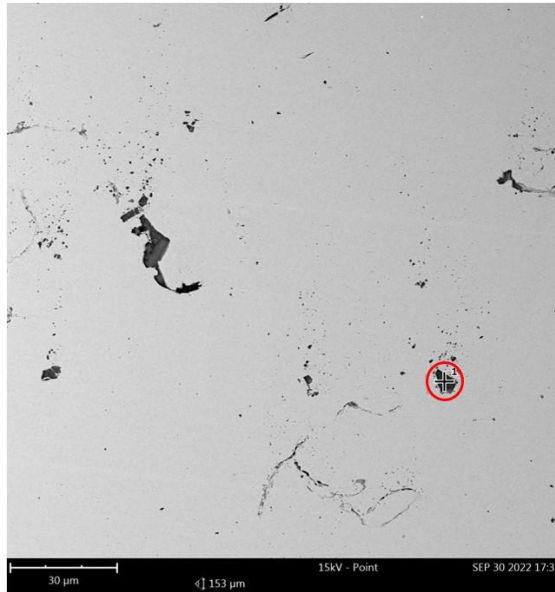


Figure 47: EDS Spot Analysis

Table 14: Element concentrations in spot of Figure 47

Element	Atomic concentration (%)	Weight concentration (%)
Silicon	100.00	100.00

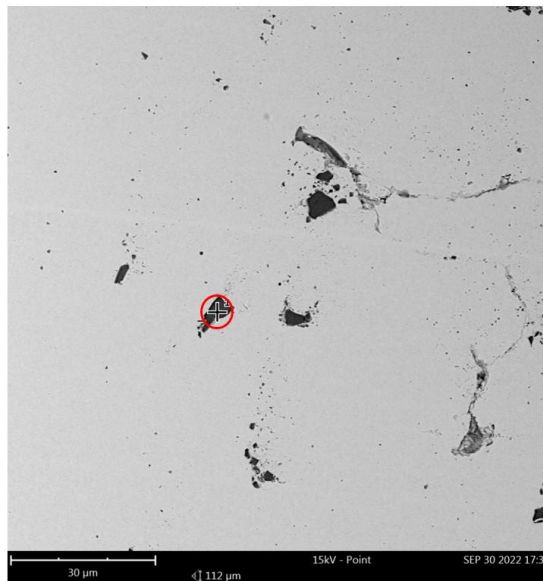


Figure 48: EDS Spot Analysis

Table 15: Element concentrations in spot of Figure 48

Element	Atomic concentration (%)	Weight concentration (%)
Silicon	100.00	100.00

7.2.2.2 Etched Images

Several different etchants and durations of etching were tried to reveal the microscopic properties of the samples. Among them the following etchants and durations revealed the properties most clearly:

- 1) 30th Etchant in ASTM E407 Standard (25% NH₄OH + 25% H₂O + 50% H₂O₂) [65]. Electro-etching for 30 seconds.

Melt-pools can be clearly observed with this etchant, evident in Figure 49. The melt-pool dimensions are in the range of 75 μm to 100 μm. Etching using this etchant can be useful for the observation and analysis of percentage of remelting of powder and defects of lack of fusion. Along with the melt-pools small black-spots can be observed which are the result of pitting during etching.



Figure 49: Melt-pool visualization (Magnification: 500X)

- 2) Nitric Acid Solution (50% HNO₃ + 50% H₂O) for 10 seconds.

The epitaxial columnar growth that is characteristic to an AM process can be seen clearly in the Figure 50 and Figure 51 with this etchant. The columnar grains are parallel to the building direction and the dimensions of these grains can reach up to a few millimetres.

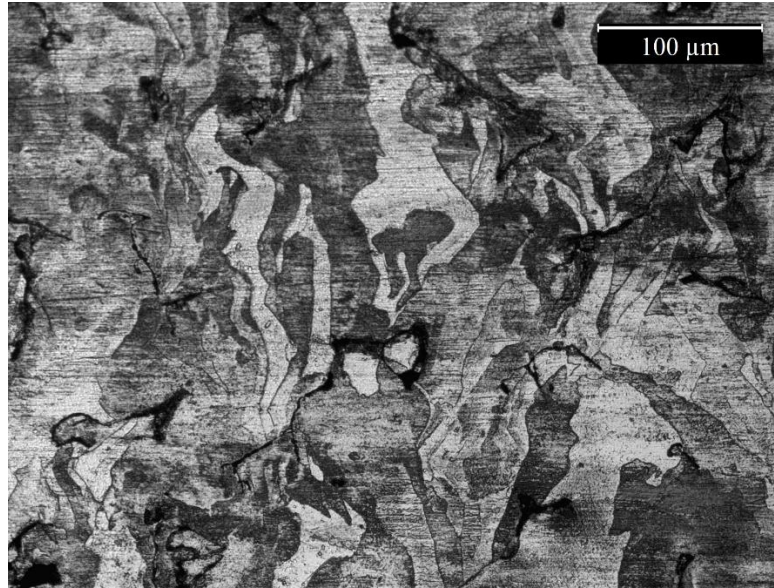


Figure 50: Columnar grain structure (Magnification: 200X)



Figure 51: Columnar grain structure (Magnification: 500X)

- 3) 40th Etchant in ASTM E407 Standard (5 grams of FeCl_3 + 16 mL HCl + 60 ml $\text{C}_2\text{H}_5\text{OH}$) [65] for 20 seconds.

This etchant could prove especially useful for observing different aspects of microstructure under the Scanning Electron Microscope. The SEM images of the sample etched with this etchant reveal detailed aspects of the orientation of the dendrites in a grain, the columnar grain growth and the melt-pools, all of which are visible in Figure 52.

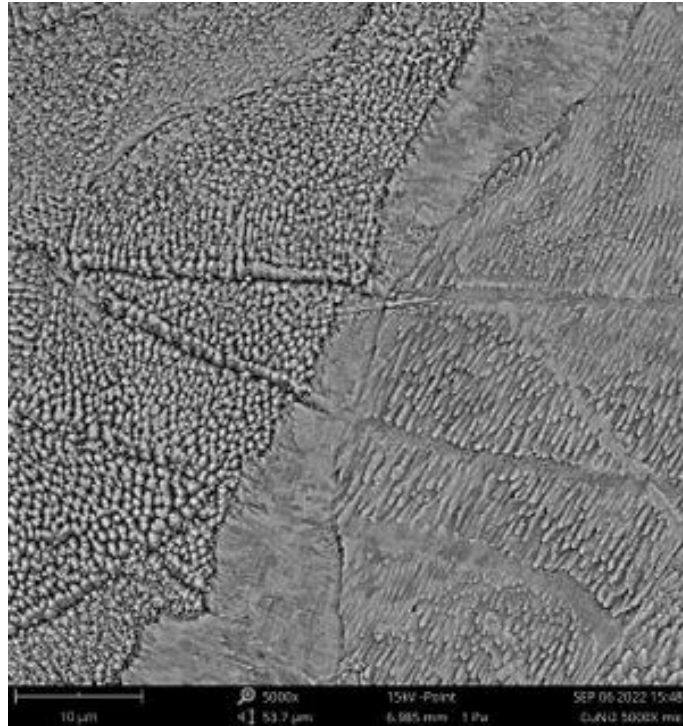


Figure 52: SEM images after etching (Magnification: 5000X)

7.2.2.3 Defects

The defects inside the microstructure are evident in Figure 53 and Figure 54. The image in Figure 53 is obtained after etching a sample with the 1st etchant mentioned in Section 7.2.2.2, while the image in Figure 54 is of an unetched sample. Un-melted powder and cracks can clearly be seen. Along with decreasing the strength of the alloy, the un-melted powder particles present a problem during polishing as well. They fall-off during polishing leaving a cavity behind which is calculated as porosity during ImageJ analysis.

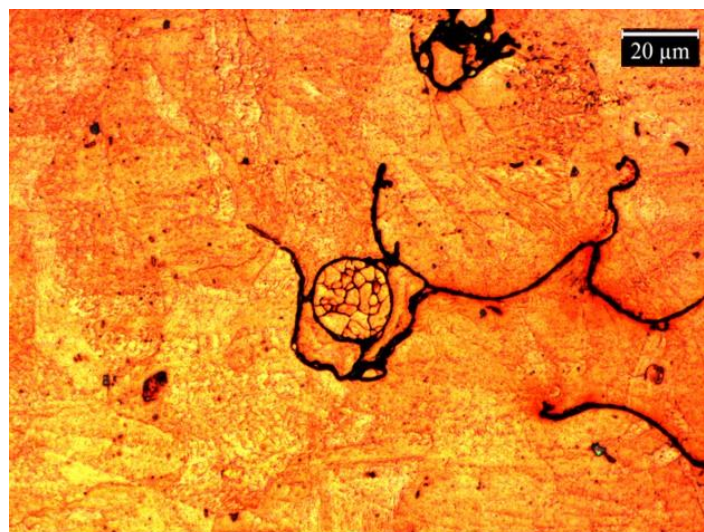


Figure 53: Un-melted powder (Magnification: 500X)

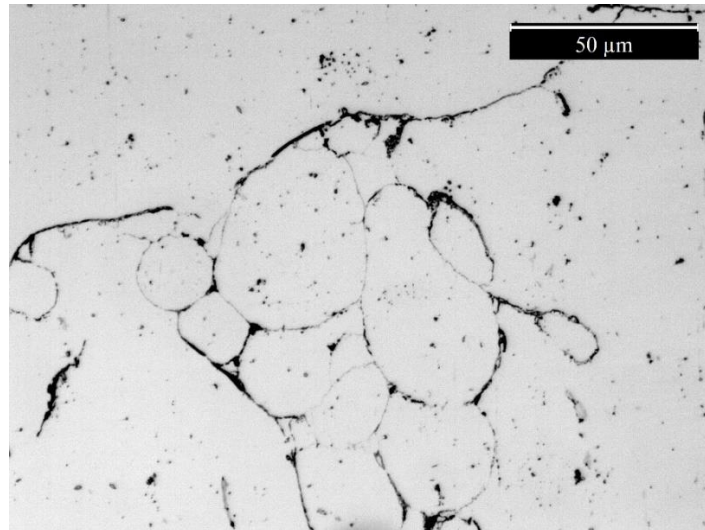


Figure 54: Un-melted powder and cracks (Magnification: 500X)

7.2.2.4 XRD Analysis

The XRD analysis shows a drastic change in intensity for the lattice-plane of [220] as can be seen in Figure 55. Such result is obtained due to the columnar grains. The unidirectional grains cause high intensity peak only for the plane perpendicular to the build direction, while not for the plane parallel to the build direction. Also, only copper is detected by comparing the obtained intensity graph with a database, as for XRD the minimum element concentration for detection is 5%. The amount of nickel in this alloy is less than that, hence it is not detected. It can be ascertained if nickel does in fact exist in solid solution with copper, by calculating the lattice parameter. A preliminary study performed on a sample for calculating the lattice parameter yielded a result of $3.6122 \pm 0.0127 \text{ \AA}$ which is a smaller value than the expected value for copper of 3.6147 \AA [66], suggesting the presence of an element with smaller atomic radii in the matrix. EDS analysis suggests the presence of Nickel in the matrix with copper. Hence, it ascertains that copper is in solid solution with nickel.

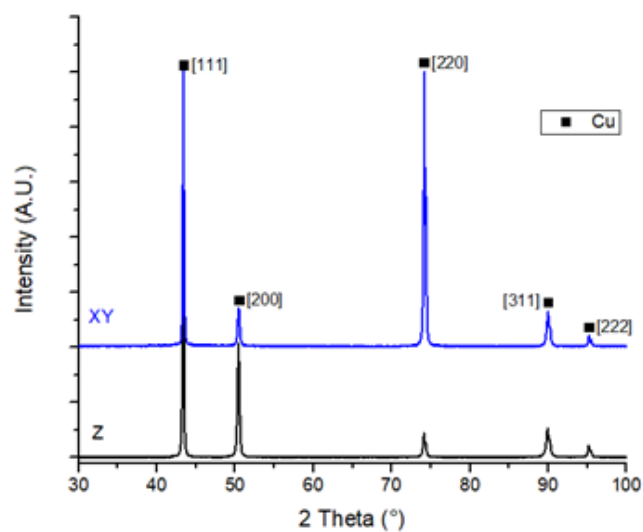


Figure 55: XRD Output graph

7.2.3 Physical properties

7.2.3.1 Tensile properties

The tensile properties of the alloy printed with the optimized process parameters were obtained by testing four dog-bone shaped samples. However, because one sample was fractured outside the gage length of the sample, the obtained properties were not considered. The values obtained from other samples are reported in Table 16 and the stress vs strain graph is shown in Figure 56.

Table 16: Tensile test values

Tensile Sample Number	Yield Strength (MPa)	Ultimate Tensile Strength (MPa)	Elongation at Break (%)
2	136	168	11
3	146	178	9
4	134	157	5
Mean	139	168	9
Standard Deviation	5	9	2

These results were compared with the tensile strength values reported in the available datasheet provided by two CuNi2SiCr powder manufacturers such as SLM solutions (Table 17) and CRP Meccanica (Table 18). The values mentioned in the 'H' rows of Table 17 are the values of the physical properties of the samples in the horizontal direction i.e., in the direction perpendicular to the build direction. While in the 'V' rows of Table 17, the values of physical properties in the build direction are reported. The values in 'H' row should be taken in consideration as the printed tensile samples for this thesis had the same orientation. Tensile samples with orientation along the build direction could not be manufactured owing to the constraint of build volume of the LPBF system used. As it can be seen in Table 5, the maximum height of the build-volume is 80 mm, while a sample of 90 mm is required for the tensile tests. It is evident that the experimental results are lower with respect to those reported in both the datasheets. For *SLM solutions* the reported relative density is greater than 99.50% [29]. The lower relative densities, due to pores and cracks in the printed samples decrease the tensile properties considerably.

Table 17: Tensile test values reported in datasheet of SLM Solutions [29]

Tensile test ^[9]			M	SD
Tensile strength	R _m [MPa]	H	314	2
		V	281	4
Offset yield strength	R _{p0,2} [MPa]	H	260	4
		V	239	2
Elongation at break	A [%]	H	36	2
		V	40	1

Table 18: Tensile test values reported in datasheet of CRP Meccanica [67]

Mechanical Properties	Test Method	As Built
Tensile Strength	DENI EN 10002	Approx. 250 ± 10 MPa
Yield Strength (Rp 0.2 %)	DENI EN 10002	Approx. 190 ± 10 MPa
Elongation at Break	DENI EN 10002	Approx. 34 ± 5 %

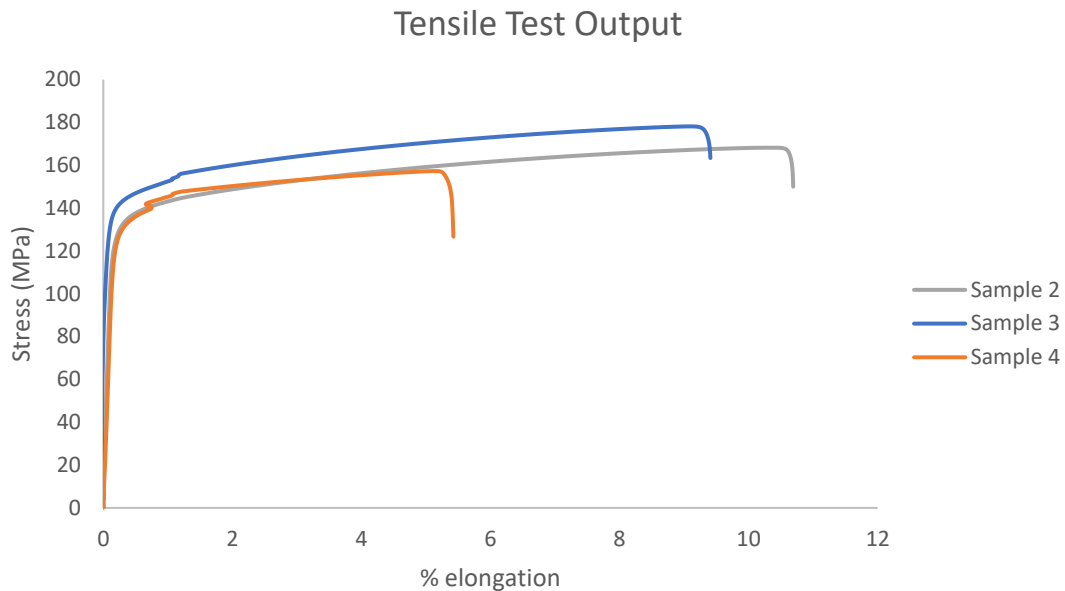


Figure 56: Tensile test plots

7.2.3.2 Hardness

Vickers Hardness test yielded a hardness value of 93 ± 11 HV. Whereas the values of hardness test performed by *SLM Solutions* is reported in Table 19. The effect of porosity was not as pronounced as the tensile strength values but was considerable. This result is reasonable and expected, as the pores and cracks collapse under load, decreasing the component's resistance to indentation [68]. The parameter of diagonal 'd' described in Section 6.8 increases thus decreasing the value of the hardness.

Table 19: Hardness test values reported in datasheet of SLM Solutions [29]

Hardness test ⁽¹⁰⁾		M	SD
Vickers hardness	HV10	105	1

7.2.3.3 Electrical properties

Some preliminary tests were performed to investigate the electrical properties of CuNi2SiCr alloy using the test method described in Section 6.10. A value of electrical conductivity equal to 6

MS/m, which is 10% IACS (International Annealed Copper Standard) was obtained. The value obtained for electrical conductivity by *SLM Solutions* is 8 MS/m, which is 14% IACS (reported in Table 20). The effect of porosity on the values of conductivity in additively manufactured materials is reported in literature [26]. Although, such research has not been performed specifically for the alloy of CuNi2SiCr, it exists for additively manufactured copper and the results are shown in Figure 57. This behaviour of decreasing electrical conductivity of pure copper with increasing porosity is the result of pores obstructing the free flow of electrons through the material. Interstitial elements in alloys also affect the conductivity in a similar way. Therefore, lower values are obtained for electrical conductivities.

Future research on electrical conductivity could investigate the conductivities of the components in the build direction. The columnar grains in the build direction provide an easier path for electrons to flow increasing the parameter [26]. Whereas in the direction perpendicular to the build-direction, the conductivity is lower as the columnar grains hinder the path of electrons.

Table 20: Electrical conductivity value reported in datasheet of *SLM Solutions* [29]

Conductivity measurement ^[5]		
Electrical conductivity	[MS/m]	8
	[%IACS]	14

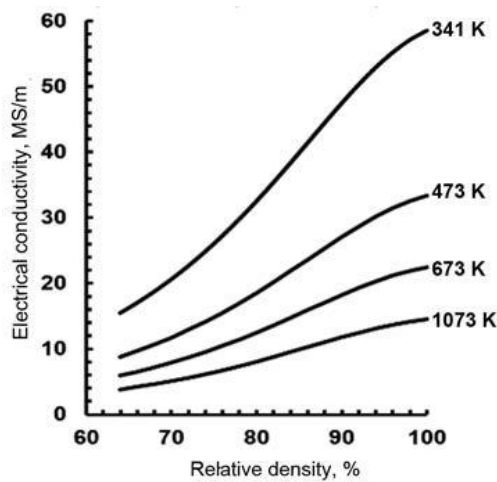


Figure 57: Effect of relative density on electrical conductivity of pure copper produced with AM [26]

A test of homogeneity was also performed where the heat dissipated in Watts from the entire length of the sample was observed by passing a current through the sample-strips. The thermal map can be seen in Figure 58. It was observed that the distribution of defects throughout the length of the sample is uniform.

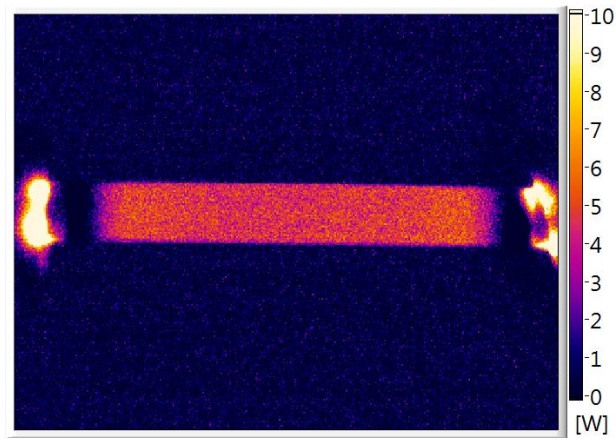


Figure 58: Test for homogeneity

8. CONCLUSION

Additive manufacturing of metals is an extremely promising technology that has revolutionized the world of production by manufacturing components with a different innovative approach. Future advancements in this technology have the potential of transforming this field of manufacturing completely. Copper is already at the forefront of these developments. With newer alloys that are produced conventionally being introduced into AM, it has a lot of untapped potential. CuNi2SiCr alloy is also one such alloy. The paucity of research on it in the literature increased the importance to investigate its characteristics when processed using AM, especially with LPBF systems. This was the main objective of this thesis which was addressed.

An average value of relative density of 97.65 ± 0.73 % was obtained with the optimized process parameters of Laser Power: 95 W, Hatch distance: 0.080 mm, Layer thickness: 0.015 mm and Scanning speed: 200 mm/s. The only available literature at the time of writing this thesis which researched on printing this alloy with a 100 W IR-laser LPBF system could achieve an average value of 94.30 % [69]. A more than 3% increase in the relative density was achieved with the process-parameters found during this thesis.

The different etchants and their respective etching time found during analysis, to reveal different aspects of the microstructure, will help in further advancing the studies on this copper alloy, which will contribute to widespread adoption of the material in the industry. The defects observed during the microstructural observation of the alloy introduces the opportunity and the need for altering the characterisation methods of polishing these types of alloys.

The trend of increasing relative density with increasing dimensions of the components could be the next interesting research point for future researchers of the field.

References

- [1] 'Charles Hull SLA invention', <https://www.historyofinformation.com/detail.php?id=3864>.
- [2] A. Gebhardt and J.-S. Hoetter, 'Rapid Tooling', in *CIRP Encyclopedia of Production Engineering*, L. Laperrière and G. Reinhart, Eds. Berlin, Heidelberg: Springer Berlin Heidelberg, 2014, pp. 1025–1035. doi: 10.1007/978-3-642-20617-7_16751.
- [3] 'AM market size predictions 2030', <https://www.grandviewresearch.com/industry-analysis/additive-manufacturing-market>.
- [4] M. Attaran, 'The rise of 3-D printing: The advantages of additive manufacturing over traditional manufacturing', *Bus Horiz*, vol. 60, no. 5, pp. 677–688, 2017, doi: <https://doi.org/10.1016/j.bushor.2017.05.011>.
- [5] W. Tao and M. Leu, *Design of lattice structure for additive manufacturing*. 2016. doi: 10.1109/ISFA.2016.7790182.
- [6] 'Advantages of AM', <https://www.jabil.com/blog/advantages-of-additive-manufacturing.html>.
- [7] 'AM advantages during Covid-19 pandemic', <https://www.tctmagazine.com/additive-manufacturing-3d-printing-news/3d-printing-companies-respond-coronavirus-crisis/>.
- [8] A. Vranić, N. Bogojevic, S. Ciric-Kostic, D. Crocchio, and G. Olmi, 'Advantages and drawbacks of additive manufacturing', *IMK-14 - Istrazivanje i razvoj*, vol. 23, pp. 57–62, Jan. 2017, doi: 10.5937/IMK1702057V.
- [9] S. Dengler, C. Kübel, A. Schwenke, G. Ritt, and B. Eberle, 'Near- and off-resonant optical limiting properties of gold-silver alloy nanoparticles for intense nanosecond laser pulses', *Journal of Optics*, vol. 14, p. 075203, Jul. 2012, doi: 10.1088/2040-8978/14/7/075203.
- [10] 'AM Power', <https://ampower.eu/download/5098/>, Mar. 2022.
- [11] M. C. Sow *et al.*, 'Influence of beam diameter on Laser Powder Bed Fusion (L-PBF) process', *Addit Manuf*, vol. 36, p. 101532, 2020, doi: <https://doi.org/10.1016/j.addma.2020.101532>.
- [12] 'EOS M 100 Additive Manufacturing System for the Fast and Efficient Production of Delicate Metal Parts Metal Solutions'. [Online]. Available: www.eos.info
- [13] C. U. Brown *et al.*, 'The effects of laser powder bed fusion process parameters on material hardness and density for nickel alloy 625', Gaithersburg, MD, Aug. 2018. doi: 10.6028/NIST.AMS.100-19.
- [14] S. Megahed, V. Aniko, and J. H. Schleifenbaum, 'Electron Beam-Melting and Laser Powder Bed Fusion of Ti6Al4V: Transferability of Process Parameters', *Metals (Basel)*, vol. 12, no. 8, p. 1332, Aug. 2022, doi: 10.3390/met12081332.
- [15] S. Sreekanth, 'Laser-Directed Energy Deposition: Influence of Process Parameters and Heat-Treatments'.
- [16] M. Mitterlehner, H. Danninger, C. Gierl-Mayer, J. Frank, and W. Tomischko, 'Study on The Influence of the Blade on Powder Layers Built in Powder Bed Fusion Processes for Additive

- Manufacturing', *BHM Berg- und Hüttenmännische Monatshefte*, vol. 165, no. 3, pp. 157–163, 2020, doi: 10.1007/s00501-020-00955-6.
- [17] D. Obilanade, C. Dordlofva, and P. Törlind, 'Surface roughness considerations in design for additive manufacturing - A literature review', in *Proceedings of the Design Society*, 2021, vol. 1, pp. 2841–2850. doi: 10.1017/pds.2021.545.
- [18] 'ELECTRON BEAM MELTING 2 GE Additive'.
- [19] 'Metal AM', <https://www.metal-am.com/articles/unrealised-potential-the-story-and-status-of-electron-beam-powder-bed-fusion-3d-printing/>, 2021.
- [20] J. Dávila, P. Neto, P. Noritomi, R. Coelho, and J. Silva, 'Hybrid manufacturing: a review of the synergy between directed energy deposition and subtractive processes', *International Journal of Advanced Manufacturing Technology*, vol. 110, Aug. 2020, doi: 10.1007/s00170-020-06062-7.
- [21] Unified Numbering System, 'Copper Alloys Classification', <https://www.unscopperalloys.org/>.
- [22] 'Copper's electrical conductivity', <https://help.leonardo-energy.org/hc/en-us/articles/207900705-Copper-sets-the-standard-for-conductivity>.
- [23] 'Copper's thermal conductivity', <http://hyperphysics.phy-astr.gsu.edu/hbase/Tables/thrcn.html>.
- [24] 'AMCM M 4K system', <https://amcm.com/machines/amcm-m4k>.
- [25] 'Copper machining with lasers', 2011. Accessed: Oct. 03, 2022. [Online]. Available: www.laser-journal.de
- [26] T. J. Horn and D. Gamzina, 'Additive Manufacturing of Copper and Copper Alloys', in *Additive Manufacturing Processes*, ASM International, 2020, pp. 388–418. doi: 10.31399/asm.hb.v24.a0006579.
- [27] 'Copper Weldability', *American Welding Society*, 1997, Accessed: Aug. 31, 2022. [Online]. Available: https://www.copper.org/publications/pub_list/pdf/a1050.pdf
- [28] 'EOS Copper Portfolio', <https://www.eos.info/en/additive-manufacturing/3d-printing-metal/dmls-metal-materials/copper>, 2022.
- [29] SLM Solutions, 'C18000 Data Sheet'. Accessed: Sep. 01, 2022. [Online]. Available: https://www.slm-solutions.com/fileadmin/Content/Powder/MDS/MDS_Cu-Alloy_CuNi2SiCr_0919_EN.pdf
- [30] Y. Zhang, 'microstructures and properties of high entropy alloys', *Prog Mater Sci*, vol. 61, pp. 1–93, Apr. 2014.
- [31] Sisma Spa, 'C18000 Data sheet'. Accessed: Sep. 01, 2022. [Online]. Available: https://www.nutechnologies.ro/public/data_files/media/brosuri/metale-slm/202006031553-datasheet_CuNi2SiCr_COMMERCIAL.pdf
- [32] 'Protolabs CuNi2SiCr Datasheet', 1999. Accessed: Aug. 31, 2022. [Online]. Available: <https://www.protolabs.com/media/1022810/copper-cuni2sicc-050321.pdf>

- [33] 'Standard Test Methods for Flow Rate of Metal Powders Using the Hall Flowmeter Funnel 1 2. Referenced Documents 2.1 ASTM Standards: 2 B215 Practices for Sampling Metal Powders B243 Terminology of Powder Metallurgy B855 Test Method for Volumetric Flow Rate of Metal Powders Using the Arnold Meter and Hall Flowmeter Funnel B964 Test Methods for Flow Rate of Metal Powders Using the Carney Funnel', doi: 10.1520/B0213-13.
- [34] 'Hall Flowmeter Apparatus', <http://www.labulk.com/astmb212-free-flowing-metal-powders-apparent-density-hall-flowmeter-funnel/>.
- [35] 'Gas Pycnometers'. Accessed: Sep. 08, 2022. [Online]. Available: https://dlu.com.ua/Files/ProductLine/Gas_Pycnometers_Brochure.pdf
- [36] 'Anton Paar Pycnometer (Model: Ultrapyc 5000)', <https://www.anton-paar.com/us-en/products/details/ultrapyc/>.
- [37] M. Bonesso *et al.*, 'Effect of Particle Size Distribution on Laser Powder Bed Fusion Manufacturability of Copper', *BHM Berg- und Hüttenmännische Monatshefte*, vol. 166, no. 5, pp. 256–262, May 2021, doi: 10.1007/s00501-021-01107-0.
- [38] 'Lecture 34 Rayleigh Scattering, Mie Scattering 34.1 Rayleigh Scattering'.
- [39] F. Storti and F. Balsamo, 'Particle size distributions by laser diffraction: sensitivity of granular matter strength to analytical operating procedures', 2010. [Online]. Available: www.solid-earth.net/1/25/2010/
- [40] 'Granulometry working principle', <https://www.thinkymixer.com/en-gl/library/report/method-of-particle-seize-evaluation-of-ground-material/>.
- [41] 'Mastersizer 3000 Smarter particle sizing'. Accessed: Oct. 04, 2022. [Online]. Available: https://www.malvernpanalytical.com/en/products/product-range/mastersizer-range/mastersizer-3000?campaignid=1525758893&adgroupid=72877486011&creative=603696199893&keyword=laser%20diffractometer&matchtype=b&network=g&device=c&gclid=EA1aIQobChMI3LTQo53G-gIVQQfmCh2xug2WEAAYASAAEgKqiPD_BwE
- [42] 'Concept Laser Mlab cusing R', <https://www.ge.com/additive/additive-manufacturing/machines/dmlm-machines/mlab-family>.
- [43] 'Mlab family'. Accessed: Sep. 08, 2022. [Online]. Available: https://www.ge.com/additive/sites/default/files/2021-11/DMLM_Mlab_Bro_4_US_EN_v1.pdf
- [44] P. Lykov, E. v Safonov, and A. Akhmedianov, 'Selective Laser Melting of Copper', *Materials Science Forum*, vol. 843, pp. 284–288, Feb. 2016, doi: 10.4028/www.scientific.net/MSF.843.284.
- [45] T.-T. Ikeshoji, K. Nakamura, M. Yonehara, K. Imai, and H. Kyogoku, 'Selective Laser Melting of Pure Copper', *JOM*, vol. 70, no. 3, pp. 396–400, 2018, doi: 10.1007/s11837-017-2695-x.
- [46] M. Colopi, L. Caprio, A. G. Demir, and B. Previtali, 'Selective laser melting of pure Cu with a 1 kW single mode fiber laser', *Procedia CIRP*, vol. 74, pp. 59–63, 2018, doi: <https://doi.org/10.1016/j.procir.2018.08.030>.

- [47] X. Yan *et al.*, 'Microstructure and mechanical properties of pure copper manufactured by selective laser melting', *Materials Science and Engineering: A*, vol. 789, p. 139615, 2020, doi: <https://doi.org/10.1016/j.msea.2020.139615>.
- [48] J. Huang *et al.*, 'Pure copper components fabricated by cold spray (CS) and selective laser melting (SLM) technology', *Surf Coat Technol*, vol. 395, p. 125936, 2020, doi: <https://doi.org/10.1016/j.surfcoat.2020.125936>.
- [49] K. Jahns, R. Bappert, P. Böhlke, and U. Krupp, 'Additive manufacturing of CuCr1Zr by development of a gas atomization and laser powder bed fusion routine', *The International Journal of Advanced Manufacturing Technology*, vol. 107, no. 5, pp. 2151–2161, 2020, doi: 10.1007/s00170-020-04941-7.
- [50] S. D. Jadhav, S. Dadbakhsh, L. Goossens, J.-P. Kruth, J. van Humbeeck, and K. Vanmeensel, 'Influence of selective laser melting process parameters on texture evolution in pure copper', *J Mater Process Technol*, vol. 270, pp. 47–58, 2019, doi: <https://doi.org/10.1016/j.jmatprotec.2019.02.022>.
- [51] C. Wallis and B. Buchmayr, 'Effect of heat treatments on microstructure and properties of CuCrZr produced by laser-powder bed fusion', *Materials Science and Engineering: A*, vol. 744, pp. 215–223, 2019, doi: <https://doi.org/10.1016/j.msea.2018.12.017>.
- [52] 'PRECISION CUT-OFF MACHINE BRILLANT 220'. Accessed: Sep. 09, 2022. [Online]. Available: https://www.qatm.com/dltmp/www/c62ebbb2-c432-4d23-9f80-52a16fc491c6-65685c7174be/brochure_cutting_brillant220_en.pdf
- [53] 'Remet compression mounting press IPA 30', <https://www.bqc.be/en/metallography/hot-mounting/mounting-presses/hot-mounting-press-ipa-30-mm/a-5849-20000432>.
- [54] 'Lapping and Polishing Machine'. Accessed: Sep. 09, 2022. [Online]. Available: <https://www.mcscorpUSA.com/wp-content/uploads/2019/02/Polishing-Machines-MECATECH-234-264-mcscorpUSA-English.pdf>
- [55] 'Leica DMI 5000M', <https://www.leica-microsystems.com/products/light-microscopes/p/leica-dmi5000-m/gallery/>.
- [56] 'SEM working principle - Purdue University', <https://www.purdue.edu/ehps/rem/laboratory/equipment%20safety/Research%20Equipment/sem.html>.
- [57] 'Alfatest Phenom XL G2 Scanning Electron Microscope', <https://www.alfatest.it/prodotti/phenom-xl-sem-da-banco>.
- [58] 'EDS working principle', <https://www.thermofisher.com/blog/materials/edx-analysis-with-sem-how-does-it-work/>.
- [59] 'XRD Working Principle', <https://cms.eas.ualberta.ca/xrd/how-xrd-works/>.
- [60] 'A REVOLUTION IN THE WORLD OF X-RAY DIFFRACTION'. Accessed: Oct. 04, 2022. [Online]. Available: <https://www.malvernpanalytical.com/en/products/product-range/empyrean-range/empyrean>
- [61] 'Vicker's Hardness Test', <https://commons.wikimedia.org/w/index.php?curid=6531452>.

- [62] 'Chongqing Scope Instruments' DHV-1000 micro-vickers hardness tester', <https://www.cqscopelab.com/products/detail/dhv-1000-dhv-1000z-digital-micro-vickers-hardness-tester.html>.
- [63] 'Zwick Roell Universal Testing Machine', <https://www.zwickroell.com/it/prodotti/macchine-di-prova-materiali-statiche/macchine-di-prova-universali-per-applicazioni-statiche/proline/>.
- [64] '4-point electrical conductivity test', <https://www.mgchemicals.com/knowledgebase/white-papers/4-point-probe/>.
- [65] 'Standard Practice for Microetching Metals and Alloys 1'. Accessed: Sep. 20, 2022. [Online]. Available:
https://edisciplinas.usp.br/pluginfile.php/4313805/mod_resource/content/1/NORMA_ASTM_ATAQUE_E407-99.28400.pdf
- [66] 'Copper physical properties', https://www.copper.org/resources/properties/atomic_properties.html.
- [67] 'CRP Meccanica datasheet for CuNi2SiCr alloy powder', https://www.crpmeccanica.com/PDF/SLM-DMLS_CopperAlloyCuNi2SiCr.pdf.
- [68] S. G. R. Brown, J. A. Cherry, H. M. Davies, S. Mehmood, N. Lavery, and J. Sienz, 'Investigation into the Effect of process parameters on microstructural and physical properties of 316L stainless steel parts by selective laser melting', *International Journal of Advanced Manufacturing Technology*, Feb. 2014, doi: 10.1007/s00170-014-6297-2.
- [69] J. Yapple, D. Bhate, B. Azeredo, and P. Phelan, 'Design and Additive Manufacturing of Copper Heat Sinks for Microelectronics Cooling', 2021.